SLAC–PUB–6571
July, 1994
(T/E)

High Energy Photon–Photon Collisions*

STANLEY J. BRODSKY

Stanford Linear Accelerator Center
Stanford University, Stanford, California 94309

and

PETER M. ZERWAS
Deutsches Elektronen-Synchrotron DESY
D-22603 Hamburg FRG

Presented at the Workshop on
Gamma-Gamma Colliders
Lawrence Berkeley Laboratory, March 28-31, 1994

**Presented at the Workshop on Gamma-Gamma Collider
Berkeley, CA , March 28-31, 1994**

* Work supported by the Department of Energy, contract DE–AC03–76SF00515.

SLAC–PUB–6571
July 1994
(T/E)

HIGH ENERGY PHOTON–PHOTON COLLISIONS*

STANLEY J. BRODSKY
Stanford Linear Accelerator Center
Stanford University, Stanford, California 94309

and

PETER M. ZERWAS
Deutsches Elektronen-Synchrotron DESY
D-22603 Hamburg FR Germany

ABSTRACT

The collisions of high energy photons produced at a electron-positron collider provide a comprehensive laboratory for testing QCD, electroweak interactions, and extensions of the standard model. The luminosity and energy of the colliding photons produced by back–scattering laser beams is expected to be comparable to that of the primary e^+e^- collisions. In this overview, we shall focus on tests of electroweak theory in photon-photon annihilation, particularly $\gamma\gamma \to W^+W^-$, $\gamma\gamma \to$ Higgs bosons, and higher-order loop processes, such as $\gamma\gamma \to \gamma\gamma, Z\gamma$ and ZZ. Since each photon can be resolved into a W^+W^- pair, high energy photon-photon collisions can also provide a remarkably background-free laboratory for studying WW collisions and annihilation. We also review high energy $\gamma\gamma$ tests of quantum chromodynamics, such as the scaling of the photon structure function, $t\bar{t}$ production, mini-jet processes, and diffractive reactions.

* Work supported in part by the Department of Energy, contract DE–AC03–76SF00515.

1. Introduction

The photon, as postulated nearly a century ago by Planck, is a discrete quantum of electromagnetic energy. The advent of TeV electron-positron linear colliders will allow the study of the collisions of beams of photons with energies a trillion times higher than those of ordinary light.

In quantum field theory, the electromagnetic field couples to all particles carrying the electromagnetic current, and thus a photon can fluctuate into virtual states of remarkable complexity [1]. At high energies, the fluctuation of a photon into a Fock state of particles of total invariant mass $\mathcal{M}$ can persist over a time of order $\tau = 2E_\gamma/\mathcal{M}^2$ – until the virtual state is materialized by a collision or annihilation with another system [2–4]. For example, in quantum chromodynamics, the photon will couple through each quark current into a spectrum of virtual meson-like color-singlet charge-zero hadronic states. The cross section for the production of hadrons in the high energy collision of two photon beams will thus resemble the cross section for the collision of ensembles of high energy mesons [5–7]. In the case of $e\gamma$ collisions, the electron can scatter on the quark Fock states of the photon, and one can study the shape and evolution of both unpolarized and polarized photon structure functions [8,9] $F_i^\gamma(x,Q^2), g_i^\gamma(x,Q^2)$ in close analogy to the study of proton structure functions in deep inelastic lepton-nucleon scattering. In electron-photon collisions where the final state is completely determined, such as $\gamma e \to eM^0$, one can measure photon–to–meson transition form factors and other exclusive channels in analogy to the transition form factors measured in exclusive electron proton processes [10].

Thus two-photon collisions can provide an important laboratory for testing many types of coherent and incoherent effects in quantum chromodynamics. In events where each photon is resolved [11] in terms of its intermediate quark and gluon states, high momentum transfer photon-photon collisions resemble hard meson-meson collisions as illustrated in Fig. 1. In the case of exclusive final states such as $\gamma\gamma \to p\overline{p}$ or meson

pairs, photon-photon collisions provide a time-like Compton microscope for measuring distribution amplitudes, the fundamental wavefunction of hadrons [12,13]. One can study detailed features of $\gamma\gamma \to t\bar{t}$ at threshold and its final state evolution. In the case of single or double diffractive two-photon events, one can study fundamental aspects of pomeron and odderon t-channel physics [14].

In addition to quarks, leptons, and $W's$, the photon couples to all particle-antiparticle pairs postulated to carry the electromagnetic current: charged Higgs, supersymmetric particles [15], etc. Thus high energy $\gamma\gamma$ collisions can provide a laboratory for exploring virtually every aspect of the Standard Model and its extensions [16–22]. Two photons can directly annihilate into W pairs [23,24] or $q\bar{q}$ pairs at the tree graph level, or pairs of gluons, pairs of photons, Z^0's, or one or more Higgs bosons through quark and W box graphs. Two real photons can couple to any even charge conjugation resonance, unless it has spin $J = 1$, in which case it can be identified via its virtual photon couplings. In $\gamma\gamma$ events where each incident photon produces a W-pair, the e^+e^- collider becomes the equivalent of a tagged WW collider, allowing the study of WW scattering and annihilation in a new domain of electroweak and Higgs physics [25–29].

All of the physics programs which we will discuss in this report appear to be experimentally feasible at a high energy linear e^+e^- collider, since by using back-scattered laser beams (see Section 2), it is expected that the $\gamma\gamma$ luminosity will be comparable to the electron-positron luminosity, and that high photon energy and polarization can be attained [30]. Thus it is clear that a central focus of investigation at the next electron-positron linear collider will be the study of photon-photon and electron-photon collisions.

2. Sources of $\gamma\gamma$ Collisions

In an e^+e^- or e^-e^- linear collider there are three main sources of photon-photon collisions. The first is the equivalent photon spectrum in which the virtual Weizsäcker–Williams bremmstrahlung has the relatively soft spectrum $G_{\gamma/e}(x,Q^2) \sim \frac{\alpha}{2\pi} \log \frac{s}{M_e^2} \frac{1+(1-x)^2}{x}$. The equivalent photon approximation applied to each of the incident leptons gives cross sections analogous to the QCD factorization formula for fusion processes in high transverse momentum inclusive reactions [6]. Virtual bremmstrahlung has been the traditional mode for studying two-photon physics at e^+e^- storage rings, and it will continue to be very important at the next generation of B-factories. By tagging the scattered electron one can also select photons with a given spacelike mass and polarization. Thus, in the case of tagged electron-electron or electron-photon collisions, the photon mass itself becomes a variable.

The low repetition rate of e^+e^- linear colliders requires very small transverse dimensions of the electron positron bunches in order to provide the necessary collision rate. As a result, the particle trajectories are bent by the strong electromagnetic fields within the bunches, giving rise to the emission of synchrotron light [31]. Depending on the geometric shape of the bunches, hard real γ spectra are generated, in particular for beams with small transverse aspect ratio. Thus beams of real photons will be automatically created in high luminosity linear colliders by the "beamstrahlung" process in which an electron going through the opposing high density bunch of positrons scatters and radiates a spectrum of nearly collinear photons [32,33]. The beamstrahlung photons are unpolarized, but the spectrum can be considerably harder than that of the corresponding equivalent photon spectrum [31].

It appears that the most advantageous way to initiate photon-photon collisions at the next linear collider will be to use a back-scattered laser beam, as pioneered by Ginzburg *et al.* [30] In this process, photons from a laser beam of eV energies are scattered against an electron or positron beam to produce a nearly collinear beam of

high energy photons.

If the laser photons and the incoming $e^{\pm}$ beams are unpolarized, the $\gamma\gamma$ luminosity of the Compton back–scattered high–energy photons depends only weakly on the invariant energy. However, the spectrum can be made hard by scattering circularly polarized laser photons on polarized electrons/positrons of opposite helicity as shown in Fig. 2. The peak of the spectrum is close to the maximum of the $\gamma\gamma$ energy at $y_{\rm max} = x_0/(1+x_0)$ where $x_0 = 4E_e\omega_0/m_e^2$ is the invariant (γe) energy–squared in units of the electron mass. To avoid non–controllable e^+e^- pair production in collisions of laser γ's with high energy γ's, x_0 must be chosen less than 4.83. Near this limit, about 80% of the e^+e^- energy is transferred to the $\gamma\gamma$ system. At the same time, the high energy photons are circularly polarized at a degree of nearly 100% in the peak region [see Fig. 3(a)].

The transfer of the linear polarization from the laser photons to the high–energy photons is also highly efficient. The degree of the linear polarization of the high–energy γ beam is described by the third component of the Stokes vector which reaches the maximum value at the upper limit of the energy transfer, $\xi_3^{\rm max} = 2\,(1+x_0)/[1+(1+x_0)^2]$ [see Fig. 3(b)]. The degree of linear polarization rises if x_0 decreases; for $x_0 = 1$ we obtain $\xi_3^{\rm max} = 4/5$, *i.e.* 80% polarization in the high-energy photon beam.

Unlike the beamstrahlung and equivalent photon processes, the effective e^+e^- and laser-induced high energy $\gamma\gamma$ luminosities can be comparable. The extraordinary energy and high luminosity of the back-scattered laser collisions promise to make two-photon physics a key component of the physics program of the next linear collider.

In principle, each of the three types of photon beams can collide with each other, so there are actually nine possible $\gamma\gamma$ collisions at a linear collider; one also has the possibility of real photons colliding with tagged virtual photons through photon-electron collisions [34].

3. Survey of Photon-Photon Collider Processes

Figure 4 illustrates many of the processes which could be studied at a high energy $\gamma\gamma$ collider.

1. The simplest reactions are the direct $\gamma\gamma$ couplings to pairs of leptons, W's, and quarks. Any energetically accessible particle which carries the electromagnetic charge, including supersymmetric and technicolor particles, can be produced in pairs. In each case, the charged line can then radiate its respective gauge partners: *e.g.*, photons, gluons, Z's as well as Higgs bosons.

2. As shown in Fig. 4b, one can produce pairs of charge-less fundamental particles in $\gamma\gamma$ collisions through quantum loop diagrams, as in the traditional light-by-light scattering box graph [35]. For example, two photons can annihilate and produce two outgoing photons or a pair of co-planar Z's through virtual W and quark loops. A pair of gluon jets can be produced through a quark box diagram. A single Higgs boson or an excited Z' can be produced through triangle graphs [36].

3. At high energies, one or both of the an incident photons can "resolve" itself as a pair of fundamental charged particles which can then interact via scattering subprocesses. Thus, as illustrated in Fig. 4c, a photon can develop into a Fock state of $q\bar{q}$ or W^+W^- or leptonic pairs, which then interact by $2 \to 2$ processes; *e.g.*, quark-quark scattering through gluon exchange or top-quark scattering through Higgs exchange [1]. In addition, one can have interactions of a directly coupled photon with the resolved constituent of the other photon.

The cross sections for a number of electroweak processes that can be studied in a high energy linear collider are shown in Fig. 5.

4. $\gamma\gamma \to W^+W^-$ Production in a $\gamma\gamma$ Collider

One of the most important applications of two photon physics is the direct production of W pairs. By using polarized back-scattered laser beams, one can in principle study $\gamma\gamma \to W^+W^-$ production as a function of the initial photon helicities as well as resolve the W helicities through their decays. The study of $\gamma\gamma \to W^+W^-$ is complimentary to the corresponding $e^+e^- \to W^+W^-$ channel, but one can also check for the presence of anomalous four-point $\gamma\gamma \to WW$ interactions not already constrained by electromagnetic gauge invariance, such as the effects due to W^* exchange.

The cross section for $\gamma\gamma \to WW$ at a TEV linear collider rises asymptotically to a constant because of the spin-one $t-$ channel exchange: $\sigma_{\mathbf{asympt}}(\gamma\gamma \to WW) \simeq 8\pi\alpha^2/M_W^2 \simeq 80$ pb. This is a rather large cross section: a linear $\gamma\gamma$ collider with a luminosity of 10-20 fb^{-}1 will produce of the order of one million W^+W^- pairs [23].

A main focus of the pair production studies will be the values of the W magnetic moment $\mu_W = \frac{e}{2m_W}(1-\kappa-\lambda)$ and quadrupole moment $Q_W = -\frac{e}{M_W^2}(\kappa-\lambda)$. The Standard Model predicts $\kappa = 1$ and $\lambda = 0$, up to radiative corrections analogous to the Schwinger corrections to the electron anomalous moment. The anomalous moments are thus defined as $\mu_A = \mu_W - \frac{e}{M_W}$ and $Q_A = Q_W + \frac{e}{M_W^2}$.

The fact that μ_A and Q_A are close to zero is actually a general property of any spin-one system if its size is small compared to its Compton scale. For example, consider the Drell-Hearn-Gerasimov sum rule [37] for the W magnetic moment: $\mu_A^2 = \left(\mu - \frac{e}{M}\right)^2 = \frac{1}{\pi}\int_{\nu_{th}}^{\infty}\frac{d\nu}{\nu}[\sigma_P(\nu) - \sigma_A(\nu)]$. Here $\sigma_{P(A)}$ is the total photoabsorption cross section for photons on a W with (anti-) parallel helicities. As the radius of the W becomes small, or its threshold energy for inelastic excitation becomes large, the DHG integral and hence μ_A^2 vanishes. Hiller and I have recently shown [38] that this argument can be generalized to the spin-one anomalous quadrupole moment as well, by considering one of the unsubtracted dispersion relations for near-forward γ

spin-one Compton scattering [39]:

$$\mu_A^2 + \frac{2t}{M_W^2}\left(\mu_A + \frac{M_2}{W}\,Q_A\right)^2 =$$

$$\frac{1}{4\pi}\int_{\nu_{th}}^{\infty}\frac{d\nu^2}{(\nu - t/4)^3}\,Im\left(f_P(s,t) - f_A(s,t)\right)\,.$$

Here $\nu = (s-u)/4$. One again sees that in the point-like or high threshold energy limit, both $\mu_A \to 0$, and $Q_A \to 0$. This result applies to any spin-one system, even to the deuteron or the ρ. The essential assumption is the existence of the unsubtracted dispersion relations; *i.e.*, that the anomalous moments are in principle computable quantities.

In the case of the W, the finite size correction is expected to be order m^2/Λ^2, since the underlying composite theory should be chiral to keep the W mass finite as the composite scale Λ becomes large [40]. Thus the fact that a spin-one system has nearly the canonical values for its moments signals that it has a small internal size; however, it does not necessarily imply that it is a gauge field.

Yehudai [24] has made extensive studies of the effect of anomalous moments on different helicity amplitude contributing to $\gamma\gamma \to W^+W^-$ cross section. Figure 6 shows the differential cross section for the process $\gamma\gamma \to W^+W^-$ in units of $\sigma_{e^+e^-\to\mu^+\mu^-}$ as a function of center mass angle for $\lambda = 0, 0.1$ and $\kappa = 1, 0.1$. The empirical sensitivity to anomalous couplings from $\gamma\gamma$ reactions is comparable and complimentary to that of $e^+e^- \to W^+W^-$.

5. Neutral Gauge Boson Pair Production in Photon-Photon Collisions

As emphasized by Jikia [41], pairs of neutral gauge bosons of the Standard model can be produced in $\gamma\gamma$ reactions through one loop amplitudes in the Standard Model at a rate which should be accessible to a high energy linear collider. For example, the

Standard Model one-loop contributions for the reaction $\gamma\gamma \to Z^0 Z^0$ is shown in Fig. 7. The computation uses the background nonlinear gauge in order to avoid four-point couplings between the ghost fields and the W fields. The ghost fields include Faddeev-Popov ghost fields as well as scalar W auxiliary fields.

A familiar example of this type of quantum mechanical process is the production of large invariant mass $\gamma\gamma$ final states through light-by-light scattering amplitudes. Leptons, quarks, and W all contribute to the box graphs. The fermion and spin-one exchange contributions to the $\gamma\gamma \to \gamma\gamma$ scattering amplitude have the characteristic behavior $\mathcal{M} \sim s^0 f(t)$ and $\mathcal{M} \sim i s f(t)$ respectively. The latter is the dominant contribution at high energies, so one can use the optical theorem to relate the forward imaginary part of the scattering amplitude to the total $\gamma\gamma \to W^+W^-$ cross section [41]. The resulting cross section $\sigma(\gamma\gamma \to \gamma\gamma)$ is of order 20 fb at $\sqrt{s}_{\gamma\gamma}$, corresponding to 200 events/year at an NLC with luminosity 10 fb^{-1}.

Figure 8 shows the effective cross section for $\gamma\gamma \to Z^0\gamma$ at an NLC assuming the back-scattered laser spectrum [41]. The rate for transversely polarized Z dominates strongly over longitudinal Z, reflecting the tendency of the electroweak couplings to conserve helicity. The cross section for $\gamma\gamma \to Z_T\gamma$ at $\sqrt{s}_{e^+e^-} = 500$ GeV is estimated by Jikia to be 32 fb, corresponding to 320 NLC events/year. As we discuss below, the channel $\gamma\gamma \to Z_T Z_T$ provides a serious background to Higgs production in $\gamma\gamma$ collisions.

6. Higgs Physics

The origin of the electroweak symmetry breaking is one of the most exciting problems in particle physics to be solved experimentally by the present or the next generation of high energy colliders.

Within the Standard Model, the electroweak symmetry breaking is induced by the

Higgs mechanism which predicts the existence of a new fundamental scalar particle with a mass below about 1 TeV. The experimental value of the electroweak mixing angle supports, qualitatively, the hypothesis that the fundamental particles remain weakly interacting up to the GUT scale, leading to a Higgs mass below 200 GeV in the Standard Model. The solution of the hierarchy problem arising in this situation suggests the supersymmetric extension of the Standard Model, expanding the scalar sector to a spectrum of at least five neutral and charged Higgs bosons.

If light Higgs bosons do not exist, the W bosons must interact strongly with each other at energies of more than 1 TeV. Novel strong interactions may give rise to the formation of resonances in the mass range above 1 to 2 TeV.

An important advantage of a photon-photon collider is its potential to produce and determine the properties of fundamental $C = +$ resonances such as the Higgs boson [42]. The present-day analog of $\gamma\gamma \rightarrow$ Higgs production is the production of narrow charmonium states. For example, the TPC$\gamma\gamma$ collaboration at PEP [43] has reported the observation of 6 η_c events, which gives $\Gamma_{\gamma\gamma}(\eta_c) = 6.4\ ^{+5.0}_{-3.4}\ KeV$. Higher luminosity facilities such as CESR or a B-factory should allow extensive measurements of $\gamma\gamma$ physics at the charm threshold.

In this section we will concentrate on the light Higgs scenario with masses below 1 TeV [44]. The light Higgs bosons can be discovered and their properties can be studied throughout the entire Higgs mass range at the proton collider LHC and at e^+e^- linear colliders in the TeV energy range. Within this environment, $\gamma\gamma$ collisions can be exploited to solve two problems. (i) The measurement of the $\gamma\gamma$ *widths of Higgs bosons* [45,46]. Since the $\gamma\gamma$ coupling to neutral Higgs particles is mediated by charged particle loops, this observable provides indirect information on the spectrum of heavy particles and their couplings to the Higgs field. (ii) It is easy to measure the *external quantum numbers* $\mathcal{J}^{\mathcal{PC}} = 0^{++}$ of the scalar Higgs bosons [47]. However, it is very difficult to verify the negative parity of the pseudoscalar Higgs boson A^0 in

the supersymmetric extension of the Standard Model. In some parts of the $\mathcal{SUSY}$ parameter space, the positive and negative parity of states can be measured by using linearly polarized photon beams [48,49] The formation of $\mathcal{P} = +$ particles requires the γ polarization vectors to be parallel while $\mathcal{P} = -$ particles require the polarization vectors to be perpendicular. Back–scattering of linearly polarized laser light provides high–energy photon beams with a high degree of linear polarization [50]. More generally, one can use polarized photon-photon scattering to study CP violation in the fundamental Higgs to two-photon couplings [47]. In the case of electron-photon collisions, one can use the transverse momentum fall-off of the recoil electron in $e\gamma \to e' H^0$ to measure the fall-off of the $\gamma \to$ Higgs transition form factor and thus check the mass scale of the internal massive quark and W loops coupling to the Higgs [51].

7. The Higgs Particle of the Standard Model

The cross section for the formation of Higgs particles in unpolarized $\gamma\gamma$ collisions,

$$\sigma(\gamma\gamma \to H) = \frac{8\pi^2}{m_H}\Gamma(H \to \gamma\gamma)\frac{m_H\Gamma_{\rm tot}/\pi}{(s-m_H^2)^2 + (m_H\Gamma_{\rm tot})^2}$$

is determined by the $\gamma\gamma$ width of the Higgs bosons. The two γ's fusing to scalar Higgs bosons have equal helicities; if polarized γ beams are employed, the cross section is to be multiplied by a factor two. For small Higgs masses $\lesssim$ 200 GeV, the Breit–Wigner coefficient is very sharp, yet beyond this range the Higgs boson of the Standard Model becomes quickly wider [52]. The experimentally observed cross section is obtained by folding the basic formation cross section with the $\gamma\gamma$ luminosity. Typical counting rates between 100 and 1,000 events per year can be achieved in these experiments (see Fig. 9). Calculations of the effects of broadening due to the back-scattered laser energy spectrum. are also given in Refs. [53], [28], and [54].

The Higgs boson decay to $\gamma\gamma$ is mediated by the loops of all charged particles [55].

The form factors $\mathcal{F}_i$ in

$$\Gamma(H \to \gamma\gamma) = \frac{G_F \alpha^2 m_H^3}{128\sqrt{2}\pi^3} \left| \sum N_C^i e_i^2 \mathcal{F}_i \right|^2$$

depend on the mass ratios $\tau = m_H^2/4m_i^2$ of the Higgs to the loop-quark masses. Light particles decouple. However, if the Higgs couplings grow with the mass of the particles, particles even much heavier than the Higgs boson do not decouple and the form factor $\mathcal{F}_i$ approaches a constant value in this limit. This applies, for instance, to the contributions of the charged leptons and quarks in a fourth family with $\mathcal{SM}$ charge assignments [46]. Interfering with the t, W amplitudes, the $\gamma\gamma$ width of the Higgs boson depends strongly on the presence of the 4th family particles. Even crude measurements of this width afford a "virtual" glimpse of the area beyond the Standard Model at energy scales much larger than the scales which are accessible directly.

The Higgs particle of the Standard Model decays below $\sim$ 150 GeV primarily to $b\bar{b}$ quarks, above $\sim$ 150 GeV to W and Z–boson pairs [52]. Since the cross section for W–pair production in $\gamma\gamma$ collisions is very large, Z decays are the appropriate decay channel to search for Higgs particles in the high mass range while top decays are difficult to extract from the overwhelming $\gamma\gamma \to t\bar{t}$ background [56].

If the Higgs bosons are detected in the $\gamma\gamma \to H \to b\bar{b}$ channel, the main background channel is the direct continuum $\gamma\gamma \to b\bar{b}$ production [45,48,57,58]. Background events from one–resolved photon events, $\gamma\gamma \to \gamma g \to b\bar{b}$ (and even more so from two–resolved photon events) can be suppressed very efficiently by choosing the maximum $\gamma\gamma$ energy not much larger than the Higgs mass; in this case the soft gluon distribution damps the background rate very strongly [48,49]. Since the cross section for the direct production of charm quark pairs is 16 times larger than for bottom quarks, excellent μ–vertex detectors must be employed to reduce these background events.

While the photons in the signal process $\gamma\gamma \to H$ have equal helicities, the continuum background production $\gamma\gamma \to b\bar{b}$ proceeds mainly through the states of opposite

γ helicities [45,46,59,58]; this is a consequence of chirality conservation in massless QCD which requires $\mathcal{J}_z = \pm 1$ for a pair of back-to-back moving $b\bar{b}$ pairs at high energies,

$$\frac{d\sigma(\gamma\gamma \to b\bar{b})}{d\cos\vartheta} = \frac{12\pi\alpha^2 e_b^4}{s_{\gamma\gamma}} \frac{\beta}{(1-\beta^2\cos^2\vartheta)^2} \times \begin{cases} 1-\beta^4 & \text{for } \mathcal{J}_z = 0 \\ \beta^2[1-\cos^2\vartheta][2-\beta^2(1-\cos^2\vartheta)] & \text{for } \mathcal{J}_z = \pm 2 \end{cases}$$

where β is the c.m. velocity of the b quarks and ϑ the c.m. scattering angle. The suppression becomes less effective if gluon radiation is taken into account. [59,58] In particular, the cross section for charm–quark production increases significantly in the $\mathcal{J}_z = 0$ channel through gluon radiation. However, employing sufficiently powerful μ–vertex detectors, the c–quark problem remains under control also in this case (see Fig. 10).

For masses of more than 150 GeV, the Higgs particles decay almost exclusively into W^+W^- and ZZ gauge boson pairs. Since the background cross section $\gamma\gamma \to W^+W^-$ is very large, the WW channel cannot be used to detect heavy Higgs bosons, and we are left with the ZZ decay channel. However, the cross section of the background channel $\gamma\gamma \to ZZ$ has turned out to be unexpectedly large [41,56,60]. This process is of higher order in the electroweak couplings, and it is mediated by a box W loop. (An estimate [41] of the magnitude of the background cross section, $\sigma(\gamma\gamma \to Z_T) \sim Z_T \sim 250$ fb can be obtained simply by scaling the $\gamma\gamma \to \gamma\gamma$ rate by the coupling $g_{WWZ}^4/e^4 \sim 11$.) In particular for high energies, the production of transversely polarized Z bosons dominates the longitudinal cross section associated with the Higgs channel by several orders of magnitude. As a result, the detailed analysis presented in Fig. 11, leads us to conclude that the Higgs signal can be detected in the ZZ channel for masses up to about 350 GeV at a 500 GeV e^+e^- linear collider facility.

8. Higgs Particles in Supersymmetric Extensions of the Standard Model

In the minimal version of the supersymmetric extension of the Standard Model, a spectrum of five Higgs bosons is predicted: two neutral scalar particles, one neutral pseudoscalar particle, and two charged particles. The charged particles can be produced in pairs in $\gamma\gamma$ collisions; the neutral particles are produced singly with the transition amplitude built-up by the scalar, spin 1/2 and the W boson loops. The pseudoscalar Higgs boson A^0 does not couple to the gauge bosons at the Born level. The $\gamma\gamma$ width of the lightest of the neutral Higgs bosons h^0, with a mass of order m_Z, is insensitive to the contributions of the $\mathcal{SUSY}$ particle loops, and the dynamics is determined by the b, t quarks and the W bosons. The heavy neutral Higgs bosons are affected by the $\mathcal{SUSY}$ particle loops only if their masses do not exceed the threshold considerably [46].

Besides the measurement of the $\gamma\gamma$ widths of these Higgs bosons [46,61], the production of Higgs bosons in linearly polarized $\gamma\gamma$ collisions can be used to discriminate the negative parity A^0 state from the scalar positive parity h^0, H^0 states [48,49]. While the polarization vectors of the two photons must be parallel to generate 0^{++} particles [$\mathcal{M}^+ \sim \vec{\varepsilon}_1 \cdot \vec{\varepsilon}_2$], they must be perpendicular for 0^{-+} pseudoscalar particles [$\mathcal{M}^- \sim \vec{\varepsilon}_1 \times \vec{\varepsilon}_2 \cdot \vec{k}_\gamma$]. Since the A^0 Higgs particle does not couple directly to gauge bosons, the measurement of the parity in $\gamma\gamma$ collisions will be a unique method in areas of the parameter space where the decay to $t\bar{t}$ pairs cannot be exploited.

Since only part of the linear laser polarization is transferred to the high-energy photon beams, it is useful to define the polarization asymmetry

$$\mathcal{A} = \frac{N^{\parallel} - N^{\perp}}{N^{\parallel} + N^{\perp}}$$

where $N^{\parallel}$ and $N^{\perp}$ denote the number of $\gamma\gamma$ events with the initial laser polarization being parallel and perpendicular, respectively. It follows that $\mathcal{A}(0^{\pm}) = \pm\mathcal{A}$. For resonance production, the asymmetry $\mathcal{A}$ can be expressed by the appropriate lumi-

nosity factors, $\mathcal{A} = \langle \Phi_3 \Phi_3 \rangle \, / \, \langle \Phi_0 \Phi_0 \rangle$, where the third component of the Stokes vector is defined as $\xi_3 = \Phi_3/\Phi_0$. The maximum sensitivity $\mathcal{A}_{\max} = (\xi_3^{\max})^2$ is reached for small values of $x_0 \lesssim 1$ and near the maximum $\gamma\gamma$ energy (see Fig. 12) [48,49].

The background continuum production $\gamma\gamma \to b\bar{b}$ dilutes the asymmetries. Because $N^{\parallel} = N^{\perp}$ in the continuum sufficiently above the threshold, the background process does not affect the numerator of the asymmetry, yet it does increase the denominator significantly, thus diminishing the observed asymmetry. Large integrated $\gamma\gamma$ luminosity of 20 to 100 fb^{-1} are necessary in general to reach statistically significant conclusions. [48,49]

Under these conditions the polarization asymmetry of the lightest neutral Higgs boson h^0 can be measured throughout the relevant parameter range, except presumably in the very low mass range, Fig. 13. The measurement of the parity in the unique case of the pseudoscalar A^0 Higgs particle appears feasible throughout most of the parameter range below the top threshold, Fig. 14. Optimization procedures in choosing the $e^{\pm}$ beam energy and the laser frequency as well as the analysis of other than $b\bar{b}$ decay channels ameliorate this picture further [48,49].

9. Studying *WW* Collisions at a Photon Linear Collider

One of the most interesting potential applications of photon-photon collisions at a high energy linear collider is WW scattering, as illustrated in Fig. 15.

In this process [25–29] each photon is resolved as a WW pair. The interacting vector bosons can then scatter pair-wise or annihilate; *e.g.*, they can annihilate into a Standard Model Higgs boson [62,63] or a pair of top quarks. In principle, one can use this process as a nearly background-free laboratory for studying WW interactions. The scattering reaction leads to two W's emerging at large transverse momentum in the final state accompanied by two W's at $p_T \sim M_W$ focussed along the beam

direction. We can estimate the cross section for $\gamma\gamma \to WWWW$ to be of order $\sigma_{\gamma\gamma\to WWWW} \sim \left(\frac{\alpha}{\pi}\right)^2 \log^2 \frac{s}{M_W^2}\, \sigma_{WW\to WW}$

The splitting function for $\gamma \to W^+W^-$ is relatively flat for some W helicities, so that one has a relatively high probability for the W's to scatter or annihilate with a high fraction of the parent $\gamma\gamma$ energy. The polarization of the colliding photons will also provide a critical tool in analyzing the experimental signals. One can also hope to utilize the fact that the polarization of the spectator $W's$ are correlated with their transverse momentum distributions and longitudinal momentum fractions.

The colliding $W's$ produced in a photon-photon collider can interact in many ways, including photon, Z, W, and Higgs exchange interactions in the t-and s-channels. The identical $W's$ also scatter via u-channel amplitudes. The oppositely-charged W's, can annihilate through a virtual photon or Z^0 or Higgs boson to final states such as $t\bar{t}$. When the W^+ and W^- annihilate into a Higgs boson, the $\gamma\gamma \to WWWW$ process is equivalent to $\gamma\gamma \to W^+W^-H \to WWWW$, which has been studied, *e.g.*, in Ref. [63]. As shown in Fig. 5 the $\gamma\gamma \to WWH$ production rate for a Higgs of mass 100 GeV is of order 0.4 pb at a 2 TeV $\gamma\gamma$ CM energy.

Even if the Higgs state does not exist, the cross section for WW collisions are still significant at TeV energies. Because of the equivalence theorem, longitudinally polarized W's inevitably become strongly interacting at TeV energies. The $\gamma\gamma \to WWWW$ and $\gamma\gamma \to WWZZ$ cross sections thus become maximally large. An interesting example of electroweak symmetry breaking occurs when a techni-ρ couples to the ZZ, ZW and WW channels. Kinematic cuts can be designed to separate the spectator and active vector bosons and possibly identify their charge state and polarization.

Cheung [29] and Jikia [27] have recently begun systematic studies of the $\gamma\gamma \to WWWW$ and $\gamma\gamma \to WWZZ$ channels based on various models for electroweak symmetry breaking. The analyses of the Born amplitudes are exact, without reliance

on the effective W approximation. Some representative total cross sections [27] for four gauge boson production in $\gamma\gamma$ collisions are shown in Fig. 5. The cross sections for some other standard e^+e^- and $\gamma\gamma$ reactions are also shown. [63,22] Note that the $\gamma\gamma \to WWZZ$ and $\gamma\gamma \to WWWW$ cross sections are larger than the corresponding $e^+e^- \to \bar{\nu}\nu WW$ and $e^+e^- \to \nu\bar{\nu}ZZ$ rates in e^+e^- collisions at the same available energy. Jikia also finds that the Higgs boson with a mass up to 700 GeV should be easily observed in a 1.5 TeV linear collider, and that the signal for a heavy (1 TeV) standard model Higgs boson can be observed at a 2 TeV linear collider. According to Cheung's estimates [29], the physics of this fundamental sector of the standard model could be explored at $\sqrt{s}_{\gamma\gamma} = 2$ TeV with a $\gamma\gamma$ luminosity as low as 10 fb^{-1}. Further studies of backgrounds and analyses of photon luminosities and kinematic cuts are clearly necessary, but one can be optimistic that measurements of WW collisions will eventually become viable at high energy linear colliders. A more complete discussion may be found in Jikia's and Cheung's contributions [27,29] to these proceedings.

10. Photon Structure Functions at the Next Linear Collider [64]

The photon structure functions measured in deep–inelastic electron–photon scattering [65,66] are one of the most interesting testing grounds for QCD. On one hand, the process is complicated enough to reveal rich non–trivial structures within the photon; on the other hand, it is still sufficiently simple to allow for a variety of exciting theoretical predictions. In contrast to the structure function of the proton, the transverse structure function of the photon is predicted to rise linearly with the logarithm of the momentum transfer and to increase with increasing Bjorken x [65]. This is a consequence of asymptotic freedom which allows for large transverse momenta in the splitting of a photon into a quark–antiquark pair. It was first shown by Witten [9] that the quark–parton prediction is renormalized by gluon bremsstrahlung in QCD to order unity and that the absolute scale of the photon structure function

is fixed by the value of the QCD coupling constant. Thus both the shape and size of the photon structure function are determined by perturbative QCD at asymptotic energies. At presently available laboratory energies, the perturbative picture must be supplemented by conjectures on the residual non-perturbative component of the structure function. These novel qualitative features of the photon structure function were born out by the pioneering $\gamma\gamma$ experiments at PETRA and PEP [67].

The high luminosities expected for LEP200 and the $e\gamma$ mode of prospective linear colliders will promote this fundamental $e\gamma$ process to an experimental instrument of high precision. Two problems can be addressed that are of general interest beyond the specifics of the $e\gamma$ process itself. (i) Since the size of the photon structure function is strongly affected by gluon radiation, the process can be exploited to measure the QCD coupling constant. At sufficiently large x, the *evolution* of the structure function can be used to extract $\alpha_s(Q^2)$ in a model independent way. The evaluation of the *absolute size* for this purpose is affected by the non-perturbative remnants in the hadronic components of the structure function. (ii) Accurate measurements of the quark and gluon distributions in the photon will allow predictions for a large number of phenomena in other fields such as the production of large transverse momentum jets, photons and heavy quark states in $\gamma\gamma$ and γN collisions [68,11]. Even the total $\gamma\gamma$ and photoproduction cross sections on nucleons may be affected significantly by the perturbative quark-gluon content of the photon [69].

11. Deep-Inelastic Electron-Photon Scattering [64]

If the photon fluctuates (see Appendix I) into a quark-antiquark pair, three different dynamical regimes can be distinguished, depending on the transverse momentum $k_\perp$ of the quarks with respect to the γ momentum. The transverse momentum determines the lifetime $\tau_* \sim 1/k_\perp$ of the fluctuation in the $q\bar{q}$ rest frame and $\tau \sim E_\gamma/k_\perp^2$ in the laboratory frame. (See Appendix II.)

(i) For $k_\perp \lesssim \mathcal{O}(\Lambda)$, Λ being the QCD scale parameter, the lifetime is long enough for the quark to travel to the confinement distance and to eventually resonate. Resonances, ρ, ω, φ can form in this situation, building up to hadronic photon component $|\gamma>_{\rm RES} = e/f_\rho|\rho> + e/f_\omega|\omega> + e/f_\varphi|\varphi> + ...$ If this state is probed deep–inelastically, the quark components have to be added up coherently, resulting in the Fock decomposition $|\gamma>_{\rm RES} \Rightarrow \sqrt{2}e/f_\rho[+\frac{2}{3}|u\bar{u}> - \frac{1}{3}|d\bar{d}> - \frac{1}{3}|s\bar{s}> + ...]$

(ii) If $k_\perp \gtrsim \mathcal{O}(\Lambda)$, the lifetime becomes too short for the quarks to form a bound state. Instead, a shower of quarks and gluons develops. The evolution of this shower is governed by the DGLAP equations modified by an inhomogeneous source term for quarks that accounts for the increased probability of the splitting $\gamma \to q\bar{q}$ if the phase space increases [70].

(iii) Finally, if $k_\perp$ is very large, the photons couples in a point-like fashion to the quarks, corrected to $\mathcal{O}(\alpha_s)$ etc. by loops and hard bremsstrahlung. This domain is described by the standard rules of perturbation theory.

The cross section for deep–inelastic scattering $e + \gamma \to e + X$ is parametrized by the transverse F_T^γ and the longitudinal F_L^γ structure functions, Fig. 16(a),

$$\frac{d\sigma}{dx\,dy} = \frac{2\pi\alpha^2 s_{e\gamma}}{Q^4}\left[1 + (1-y)^2\right]\left[2xF_T^\gamma(x,Q^2) + \varepsilon_y F_L^\gamma(x,Q^2)\right] .$$

The transverse structure function can be substituted by the more familiar structure function $F_2^\gamma = 2xF_T^\gamma + F_L^\gamma$. The Bjorken variable x and y can be expressed in terms of the momentum transfer Q^2, the invariant hadronic energy W, and the laboratory energies and electron scattering angle,

$$x = \frac{Q^2}{2q\cdot p_\gamma} = \frac{Q^2}{Q^2 + W^2} \quad \text{and} \quad y = \frac{q\cdot p_\gamma}{k\cdot p_\gamma} = 1 - \frac{E'}{E}\cos^2\frac{\vartheta}{2} .$$

Since the degree of the longitudinal (virtual) photon polarization is given by $\varepsilon_y = 2(1-y)/[1+(1-y)^2]$, F_2^γ comes with a coefficient $\sim (1-y)$ for small y and is easy

to measure. By contrast, F_L^γ comes with a coefficient y^2 which is difficult to measure since y must be restricted to small values to reject beam–gas background events [71].

The area in Q^2 and x that can be explored by LEP200 and a e^+e^- linear collider at a c.m. energy of 500 GeV [LC500] is characterized by a parallelogram in the $\mathcal{P} = \{\log Q^2, \log(1/x-1)\}$ plane, Fig. 17. Below the one–pion line "π" the photon structure functions vanish identically while the continuum extends from the "$\pi\pi$" threshold into the upper half of $\mathcal{P}$. The right boundary $Q^2_{\max}$ is set by experimental counting rates; $Q^2_{\max}$ is in general much smaller than $s^{\max}_{e\gamma}$. The parallelogram extends to the left down to $Q^2_{\min}$, identified in Fig. 17 with the limit below which the application of perturbative QCD becomes doubtful; similarly the base–line of the parallelogram which corresponds to $W^2_{\min}$, while the upper boundary is given by the experimentally accessible $W^2_{\max}$. Rough estimates of $Q^2_{\max}$ and $x_{\min}$ in the perturbative regime are displayed in Table 1 for LEP200 [71] and LC500. The LC500 machine has been assumed to operate in the $e\gamma$ mode so that the Q^2, x range is not only extended by the higher energy but also by the higher luminosity compared with LEP.

Table 1

	$Q^2_{\max}$	$x_{\min}$
LEP200	10^3 GeV^2	10^{-3}
LC500	10^5 GeV^2	10^{-5}

As a result of asymptotic freedom, the photon structure function $F_2^\gamma(x, Q^2)$ rises with $\log Q^2$ and also with Bjorken x [65]. The rise of the amplitude $\gamma^*\gamma \to \bar{q}q$ in x is damped by gluon radiation at intermediate to large x while the structure function increases by quark–antiquark pair creation at small x [9]. This leading logarithmic analysis has been extended to *NLO* [72] so that a complete perturbative analysis is available which can be confronted with experimental data. A crude estimate of the accuracy expected at LEP200 is displayed in Fig. 18.

In the leading asymptotic solution spurious singularities are encountered at $x \to 0$. They are induced by poles in the moments of the structure function whenever the anomalous dimensions $d_n^j (j = \pm, NS)$ approach the values $l = -1, 0, +1...$ [73] These poles are due to infrared singularities at $\mathcal{O}(\alpha_s^l)$ which are cancelled by perturbative infrared singularities at the real γ vertex. A scheme for the regularization of these singularities has been designed in Ref. [74]; *in praxi* the residual effects due to the regularization at $\mathcal{O}(\alpha_s^{-1})$ and $\mathcal{O}(1)$ are confined to small x values $\lesssim 0.15$.

Since in the present context we are only interested in gross features of the photon structure functions, we will illustrate the main points in the framework of the LO GLAP equations [75] for the moments of the parton densities in the photon, $q = \int dx\, x^{m-1} q(x, Q^2)$ etc.,

$$\frac{\partial q}{\partial t} = e_q^2 d_B + \frac{\alpha_s(t)}{2\pi} [A_{qq} * q + A_{qg} * G]$$

$$\frac{\partial G}{\partial t} = \frac{\alpha_s(t)}{2\pi} [A_{gq} * q + A_{gg} * G]$$

where $t = \log Q^2/\Lambda^2$ and $\alpha_s(t) = 1/bt$ [76].

The structure function is given, as usual, by

$$F_2^\gamma(x, Q^2) = 2 \sum_{fl} e_q^2 x q(x, Q^2)$$

the sum running over the light quark species u, d, s. The quantities d_B etc. are defined in Ref. [77]. For the non-singlet component $q = q_{2/3} - q_{1/3}$, the difference of up and down type parton densities, the solution for the evolution $t_0 \to t$ can be cast into two different forms,

$$q(t) = q(t_0) \left[\frac{\alpha_s(t)}{\alpha_s(t_0)}\right]^{d_{NS}} + \frac{1}{3} \frac{d_B}{1 + d_{NS}} \left\{ t - \left[\frac{\alpha_s(t)}{\alpha_s(t_0)}\right]^{d_{NS}} t_0 \right\}$$

$$= \{q(t_0) - q_{pt}(t_0)\} \left[\frac{\alpha_s(t)}{\alpha_s(t_0)}\right]^{d_{NS}} + \frac{1}{3} \frac{d_B}{1 + d_{NS}} \frac{2\pi/b}{\alpha_s(t)} .$$

The last term

$$q_{pt}(t) = \frac{1}{3}\,\frac{d_B}{1+d_{NS}}\frac{2\pi/b}{\alpha_s(t)}$$

denotes the "point-like component", renormalized by the anomalous dimension d_{NS} to $\mathcal{O}(1)$ with respect to the quark-parton term $\frac{1}{3}d_B \log Q^2/m_q^2$ [78]. The difference between the full solution and the point-like component, $q - q_{pt}$, will suggestively be referred to as the "hadron-like component" of the photon.

While the hadron-like component approaches zero asymptotically for $1 + d_{NS} > 0$, the point-like component grows $\sim \log Q^2$. This is a consequence of asymptotic freedom which damps the gluon radiation. Indeed, for a fixed coupling constant α_*, the quark density would approach a finite limit $q \sim \alpha_*^{-1}$ asymptotically [77], Fig. 19. The data [79] at presently available values of Q^2 are compatible with a linear rise in $\log Q^2$, Fig. 20.

The most characteristic behavior of the photon structure function $F_2^\gamma(x, Q^2)$ in QCD is its continuous linear rise of with $\log Q^2$ at fixed x. As emphasized in Ref. [77], the fact that this tree graph behavior is preserved to all orders in perturbation theory is due to the balance in QCD between the increase of the phase space for gluon emission in the scattering processes versus the decreasing strength of the gluon coupling due to asymptotic freedom. Although the logarithmic rise of the Born approximation result is preserved, the shape in x is modified by the QCD radiation.

The heavy c, b and t quark contributions are added as Born terms plus the standard QCD loop corrections [80,81]. Since $x \leq x_{\max} = Q^2/(Q^2 + 4m_q^2)$, the heavy quark threshold traverses the entire x range from low to very high Q^2. By measuring the cross section for tagged c-quark production in on-shell $\gamma\gamma$ collisions, it can be checked experimentally whether the perturbative QCD calculations [57] are trustworthy already for c quarks.

A comparison of the QCD predictions given by Laenen *et al.* [81] with data from the PLUTO experiment at PETRA for the photon structure function at $\langle Q^2 \rangle = 5.9$

GeV^2 is shown in Fig. 21. The underlying contribution due to charm at leading and higher order is also shown. The shape and normalization of the structure functions predicted by PQCD appears to be consistent with experiment although the detailed results depend on the assumed shape of the photon's gluon distribution.

11.1 Measurement of $\alpha_s(Q^2)$

For high moments, or equivalently high values of x, the parton densities are determined by the valence quark distributions in the photon which for light quarks come in the ratio $u : d : s = 4 : 1 : 1$. In this range the evolution equations can be applied directly to F_2^γ,

$$Q^2 \frac{\partial F_2^\gamma}{\partial Q^2} = \frac{4}{9} d_B - \frac{d_{NS} F_2^\gamma + \mathcal{O}(G/q)}{\log Q^2/\Lambda^2}$$

with the solution

$$F_2^\gamma(Q^2) = F_2^\gamma(Q_0^2) \left[\frac{\log Q_0^2/\Lambda^2}{\log Q^2/\Lambda^2}\right]^{d_{NS}} + \frac{4}{9} \frac{d_B}{1+d_{NS}} \left\{ \log \frac{Q^2}{\Lambda^2} - \left[\frac{\log Q_0^2/\Lambda^2}{\log Q^2/\Lambda^2}\right]^{d_{NS}} \log \frac{Q_0^2}{\Lambda^2} \right\}.$$

In analogy to the proton structure function the sensitivity of F_2^γ to Λ is due to the onset of the asymptotic behavior [82]. This is a consequence of the fact that $F_{2pt}^\gamma(Q^2) - F_{2pt}^\gamma(Q_0^2) \sim \log Q^2/Q_0^2$ is independent of Λ^2. The sensitivity of the slope $Q^2 \partial F_2^\gamma/\partial Q^2$ to Λ is illustrated in Fig. 22a. If $\Lambda_{\overline{MS}}^{(4)}$ can be determined within an error of $\pm$ 150 MeV, the error on the reference coupling $\alpha_s(m_Z^2)$ will be about 8%.

The relative strength of the hadron-like component of photon structure function approaches zero asymptotically, and the absolute magnitude of F_2^γ is given by the Λ parameter in the point-like component,

$$F_2^\gamma(Q^2) = \left\{ F_2^\gamma(Q_0^2) - F_{2pt}^\gamma(Q_0^2) \right\} \left[\frac{\alpha_s(Q^2)}{\alpha_s(Q_0^2)}\right]^{d_{NS}} + F_{2pt}^\gamma(Q^2)$$

$$F_{2pt}^\gamma(Q^2) = \frac{4}{9} \frac{d_B}{1+d_{NS}} \log \frac{Q^2}{\Lambda^2}$$

For any foreseeable energies however the hadron-like component does affect the absolute size of F_2^γ [83]. Theoretical estimates of the hadron-like component span between

two extreme hypotheses. On one side it has been assumed (see Ref. [75]) all that for sufficiently small $Q_0^2 = \mathcal{O}(1\ \mathrm{GeV}^2)$ the entire structure function $F_2^\gamma(Q_0^2)$ is given by the VDM contribution. In this case there is little sensitivity to Λ, for the same reason as before. In the other extreme case the perturbative effects are assumed to prevail down to $Q_0 \gtrsim \mathcal{O}(\Lambda)$ and the difference between $F_2^\gamma(Q_0^2)$ and $F_{2pt}^\gamma(Q_0^2)$ is attributed to the VDM component of the photon. If this difference is indeed correctly described by the ρ, ω, φ vector mesons, say to within $\pm$ 50%, the measurement of the photon structure function at $Q^2 \sim 100\ \mathrm{GeV}^2$ can be used to determine Λ with an error of about $\pm$ 120 MeV, Fig. 22b. Since the x and Q^2 dependence of $F_2^\gamma(x, Q^2)$ are predicted, this hypothesis can be scrutinized experimentally. Taking the photon target slightly off–shell, another check is provided by the P^2 dependence of the VDM contribution [84].

11.2 q/g decomposition of the photon

The *quark* decomposition of the photon cannot be disentangled in inclusive measurements at low energies, since only the sum of the parton densities weighted by their electric charges, $F_2^\gamma = 2x[\frac{4}{9}u + \frac{1}{9}d + \frac{1}{9}s + ...]$, is accessible this way. Apart from the difficult analyses of baryons in the current jet, the semi-inclusive measurement of mesons, built–up by s quarks, can be used to isolate the $q_{1/3}$ component: $K^0 = (d\bar{s}), \varphi = (s\bar{s}), ...$

Increasing Q^2 to $\sim 10^3\ \mathrm{GeV}^2$ and beyond, the virtual γ exchange is supplemented by Z–boson exchange [85], accounted for by substituting

$$e_q^2 \to \frac{1}{4} \sum_{i,j=L,R} \left[e_q - \frac{q^2}{m_Z^2 + Q^2} \frac{Z_i(e) Z_j(q)}{\sin_2 \vartheta_W \cos^2 \vartheta_W} \right]^2$$

where the electroweak Z charges are given by $Z_L(f) = I_{3L}(f) - e_f \sin^2 \vartheta_W$ and $Z_R(f) = -e_f \sin^2 \vartheta_W$ for the left– and right–handed Z couplings. A quantitative analysis of the size of this effect is presented in Ref. [85].

In addition to these $\mathcal{NC}$ mechanisms, the charged current processes $e^{\mp}+\gamma \to \nu+x$, Fig. 16(b), become important at high energies. Since the virtual W^- boson can be absorbed only by $u, \overline{d}, \overline{s}...$ quarks, and W^+ by $\overline{u}, d, s...$, the cross sections are given, both, by

$$\sigma(e\gamma \to \nu X) = \frac{G_F^2 s_{e\gamma}}{2\pi} \int dx\, dy \left[\frac{m_W^2}{m_W^2+Q^2}\right]^2 x[u+(1-y)^2(d+s)+...]$$

The total cross sections, as well as the y dependence, provide a combination of parton densities different from the $\mathcal{NC}$ process so that the $q_{2/3}$ and $q_{1/3}$ densities can in principle be disentangled. For LEP200 the cross sections are small, $\sim$ several $10fb$; they increase however to $\mathcal{O}(1pb)$ at LC500 producing several thousand charged current events. Since the Weizsäcker–Williams γ spectrum is continuous and soft, the analysis of the y dependence would be very difficult at LEP200, it is however easy in the back-scattered laser $e\gamma$ mode at LC500 where the γ spectrum peaks at high energies for polarized beams.

The *gluon* component of the photon can be measured in deep inelastic $e\gamma$ scattering only indirectly. In analogy to eN scattering, the evolution of the γ structure function $F_2^\gamma(Q^2)$ is affected by the gluon density in the following way,

$$t\frac{\partial F_2^\gamma}{\partial t} = F_{2\,box}^\gamma - d_{NS}F_2^\gamma + \frac{(2\sum_{fl} e_q^2)Aqg}{2\pi b}G\ .$$

This method appears to work well for proton targets and it should also provide valuable information on the gluon content of the photon in particular for low x values. Other measurements of G are based on jet production in resolved γ processes at HERA [68], inelastic Compton scattering mediated by resolved photons [86], as well as photoproduction of heavy quark states [11].

11.3 Small-x phenomena

The fact that in the basic photon splitting process $\gamma \to q\overline{q}$ the transverse momentum is not limited leads to two interesting questions: (i) The strong ordering along

the gluon chain in the standard DGLAP analysis associates high energy jets in the evolution with small transverse momenta. In contrast, this rule does not apply to the perturbative pomeron in the BFKL domain at very small x for moderate Q^2 [87]. It is therefore an interesting experimental problem to investigate the correlation between jet energies and transverse momenta in deep inelastic scattering $e\gamma \to e +$ jets, exploiting the difference between the initial parton configurations in the photon and the nucleon. (ii) Large transverse momenta in $\gamma \to q\bar{q}$ correspond to a small transverse size of the $(q\bar{q})$ pair in space. This leads to a high density of the gluons emitted subsequently which is eventually stopped by screening effects. Screening effects associated with the standard confinement radius R of the hadronic γ component have been analyzed in Ref. [88].

12. Polarization Effects in $\gamma\gamma$ Collisions [64]

Weizsäcker–Williams photons, as well as back–scattered laser photons, can be generated in a variety of polarization states. Weizsäcker–Williams photons are automatically polarized linearly in the production plane. If the initial $e^{\pm}$ beams are circularly polarized, part of the polarization is transferred to the photons. (See Section 2.) The degree of polarization is determined in both cases by the fraction ζ of energy transmitted from the $e^{\pm}$ beams to the photons,

$$\text{(i) linear polarization} : \varepsilon(\zeta)_{WW} = 2(1-\zeta)/[1+(1-\zeta)^2]$$

$$\text{(ii) left} - -\text{right asymmetry} : A(\zeta)_{WW} = (2-\zeta)\zeta/[1+(1-\zeta)^2] \, .$$

For back–scattering of laser photons [89], the spectrum is given by $dN/d\zeta \sim \phi_0 + \lambda_e \lambda_\gamma \phi_1$, with

$$\phi_0 = \frac{1}{1-\zeta} + 1 - \zeta - 4r(1-r)$$

$$\phi_1 = x_0 r(1-2r)(2-\zeta)$$

and $r = x_0^{-1}\zeta/(1-\zeta) \leq 1$; x_0 being the square of the invariant (γe) energy in units

of the electron mass which in general is chosen between ~ 1 and ~ 4. The degree of polarization of the high energy γ beam follows from

$$\text{(i) linear polarization} : \xi_3 = \phi_3/\phi_0 \quad \text{with} \quad \phi_3 = 2r^2$$

$$\text{(ii) left} - - \text{right asymmetry} : A = (\lambda_e\phi_4 + \lambda_\gamma\phi_5)/(\phi_0 + \lambda_e\lambda_\gamma\phi_1)$$

$$\text{with } \phi_4 = x_0 r[1 + (1-\zeta)(1-2r)^2]$$

$$\text{with } \phi_5 = (1-2r)[1/(1-\zeta) + 1 - \zeta] \, .$$

Spectra and asymmetries are displayed for the two cases in Fig. 3.

12.1 The Longitudinal photon structure function

Massless quarks which absorb a longitudinally polarized virtual photon must have non–zero transverse momenta. This is a consequence of angular momentum conservation since the $\gamma q\bar{q}$ vertex is helicity–conserving. Non–zero transverse momenta are generated in the point-like $\gamma \to q\bar{q}$ splitting process [90] and by gluon radiation off the quark beam [91]. For the first mechanism the absorption rate is of order $\int dk_\perp^2/k_\perp^2 \cdot k_\perp^2/Q^2 = \mathcal{O}(1)$, in the second case $\sim N(Q^2)\alpha_s(Q^2) = \mathcal{O}(1)$. Both contributions are therefore scale–invariant in leading order. The quark–parton diagram provides the dominant contribution, for light quarks

$$F_L(x,Q^2) = \frac{12\alpha}{\pi}\sum_{fl} e_q^4 x^2(1-x)$$

$$+ \frac{\alpha_s(Q^2)}{2\pi}\int dy\, dz\; \delta_1(x-yz)z^2\left[\frac{8}{3}F_2^\gamma + \frac{4}{3} < e_q^2 > yG(1-z)\right] \, ,$$

to which the contribution of heavy quarks, corrected by gluon loops and gluon radiation, must be added [80, 81].

A linear collider can also provide a clear and simple test of QCD in the case where both electrons are tagged at large momentum transfer so that both photons are virtual. The leading contributions to the photon structure functions take on the point-like form characteristic of the direct photon couplings to the quarks.

12.2 Linear γ polarization

The linear γ polarization gives rise to an azimuthal asymmetry of the $[e, e']$ scattering plane with respect to the polarization vector, $d\sigma/d\phi \sim \cos 2\phi \cdot \varepsilon F_\chi(x, Q^2)$. In the quark–parton model [90] the structure function F_χ is scale invariant,

$$F_\chi = -\frac{3\alpha}{\pi} \sum e_q^4 \cdot x^3 \ ,$$

modified to $\mathcal{O}(\alpha_s)$ by QCD corrections.

12.3 The polarized photon structure functions

As in the case of $\vec{e}\vec{p}$ scattering, the spin structure function $g_1^\gamma(x, Q^2)$ of the photon is measured by the asymmetry of right/left–polarized electrons scattered off polarized targets. This structure function has been recognized as a very interesting physical observable [92], which is deeply connected with the chiral properties of QCD. For sufficiently large Q^2, the spin structure function $g_1^\gamma(x, Q^2; P^2)$, P^2 denoting the mass squared of the target photon, fulfills the following sum rules

$$\int_0^1 dx g_1^\gamma(x, Q^2; P^2) = \begin{cases} 0 & \text{for } P^2 = 0 \\ N_C \frac{\alpha}{\pi} \sum_{fl} e_q^4 \left[1 + \mathcal{O}(\log^{-1} Q^2, \log^{-1} P^2)\right] & \text{for } P^2 \text{ large} \end{cases}$$

The first moment of g_1^γ is given by the matrix element $\langle \gamma | j_{5\mu} | \gamma \rangle$ which, in the free case, counts the difference between right– and left–handedly polarized quarks in the photon. In QCD this matrix element is built–up by two elements, the axial anomaly accounted for by the perturbative quark–loop contributions, and hadronic contributions by the Goldstone bosons associated with the spontaneous breaking of chiral symmetry. [This discussion also applies to the singlet axial current modulo logarithmic corrections.] Electromagnetic current conservation leads to the cancellation of the two contributions for $P^2 = 0$. For P^2 large, on the other hand, the hadronic contribution vanishes to $\mathcal{O}(1/P^2)$, and the non–zero value of the first moment of the spin structure function is entirely due to the anomaly.

13. Jet Physics at a Photon Linear Collider

The distinction between the direct, versus resolved, hadron-like contributions to photon interactions becomes especially clear in two-photon jet physics. If both photons couple directly to a pair of quarks, the final state is similar to that of e^+e^- annihilation: two co-planar jets are produced without any source of hadronic spectators emitted along the beam direction. Such events would be extraordinarily rare at an the analogous meson-meson collider.

In the case of once-resolved processes, one photon scatters directly on a constituent quark of the other photon, leaving spectators just in one beam direction. In the case of twice-resolved two-photon processes, jets are produced by any of the various qq qg and gg QCD 2 to 2 scattering subprocesses. Despite their markedly different origins, the cross sections for these two photon jet production processes are all scale invariant in leading order [11,93]; that is, in leading logarithm approximation, they each have the form:

$$\frac{d\sigma}{d^3p/E}\,(\gamma\gamma \to \text{Jet} + X) = \frac{\alpha^2}{p_T^4}\,F(x_T, \theta_{cm})\ .$$

The logarithmic fall-off of the subprocess cross section is precisely compensated by the increasing strength of the resolved photon structure function. The $x_T = 2p^{\text{jet}}/\sqrt{x}$ dependence of $F(x_T, \theta_{cm})$ has a power-law fall-off at large x_T: $\sim (1 - x_T)^N$ where the index N can be computed at $x \sim 1$ simply by counting the number of beam spectators [11].

An illustration of the various contributions to the jet transverse momentum distribution from direct, single and twice resolved contributions as calculated by Drees and Godpole is shown in Fig. 23 [11]. The dotted curve shows the background from e^+e^- annihilation events with single hard photon radiation from the initial state. A recent comparison of these predictions for single jet and two jet processes with TRISTAN data [94] obtained from thrust and other jet variable analyses appear to confirm the

presence of both direct and resolved contributions, although there are uncertainties from higher order corrections to the jet rate normalization and the assumed form of the photon's gluon distribution. The largest uncertainty in these results is due to the unknown form of the gluon distribution within the resolved photon [11,95].

14. Contribution from Mini-Jets to the $\gamma\gamma$ Cross Section

One of the uncertainties concerning QCD predictions for photon- photon collisions is the size of the total inelastic cross section which can be attributed to from mini-jets, *i.e.*, jets of p_T beyond a cutoff of order of a few GeV. Early work by Drees and Godpole [11] had suggested that the production rate for mini-jets could rise so fast with energy that mini-jets would provide a significant and troublesome minimum bias background to the study of e^+e^- events at an NLC. However, recent analyses by Forshaw and Storrow [96] and by Chen, Barklow, and Peskin [97] have now shown that the rise of the mini-jet rate is moderate into the TeV linear collider regime, and that the resulting backgrounds to physics signals are in fact minimal.

The new analyses [96,97] are based on a two-component form for total inelastic cross sections: an energy-independent term σ_0, plus a rising PQCD contribution obtained by integrating $2 \rightarrow 2$ QCD processes from $p_{t\,\mathrm{min}} = 3.2$ GeV to the kinematic limit. This parameterization is consistent with the measured rate of mini-jets measured by UA1, the energy dependence of the $p\bar{p}$ cross section, as well as $\sigma_{\gamma p}(s)$ determined by the ZEUS collaboration at HERA. The cross section for mini-jets must be unitarized so that the integral of the cross section $d\sigma/dy$ is normalized to inelastic cross section times the average multiplicity of mini-jets $\langle n \rangle$. As shown in Fig. 24 [96], the eikonalization of the subprocess cross section leads to a significant reduction in the predicted value and a rise with energy of the $\gamma\gamma$ inelastic cross section. The net result for the number of jets with $p_T > 5\ GeV$ produced per crossing at an NLC is only of order 5 to 8 $\times 10^{-2}$ for typical linear collider designs.

The physics of unitarization has been analyzed from a different perspective by Ginzburg, Ivanov and Serbo [98]. In the regime $s_{\gamma\gamma} >> p_T^2 > \mu^2$, where μ is the confinement scale of QCD, one can apply perturbative QCD to compute the set of gluon exchange chains representing the QCD Pomeron, as in Lipatov's well-known work. It is also possible to compute the double diffractive contribution where two gluon chains to recombine leaving a rapidity gap between the di-jets. Ginzburg *et al.* argue that eikonalization must be taken into account when the rates for these two processes become equal. With this assumption, they find that eikonal corrections must be applied to the perturbative QCD factorized predictions for the jet production cross section at $\sqrt{s_{\gamma\gamma}} = 500$ GeV even at jet transverse momentum as large as $p_T = 26$ GeV.

15. Single and Double Diffraction in Photon-Photon Collisions

The high energies of a $\gamma\gamma$ collider will make the study of double diffractive $\gamma\gamma \to V^0V^0$ and semi-inclusive single diffractive processes $\gamma\gamma \to V^0X$ in the Regge regime $s >> |t|$ interesting. (See Fig. 25.) Here $V^0 = \rho, \omega\phi, J/\psi, \cdots$ If $|t|$ is taken larger than the QCD confinement scale, then one has the potential for a detailed study of fundamental Pomeron processes and its gluonic composition [14,99]. As in the case of large angle exclusive $\gamma\gamma$ processes, the scattering amplitude is computed by convoluting the hard scattering PQCD amplitude for $\gamma\gamma \to q\bar{q}q\bar{q}$ with the vector meson distribution amplitudes. As shown by Chernyak and Zhitnitsky [100], the two gluon exchange contribution dominates in the Regge regime, giving a characteristic exclusive process scaling law of order $\frac{d\sigma}{dt}(\gamma\gamma \to V^0V^0) \sim \alpha_s^4(t)/t^6$. Recently, Ginzburg *et al.* [14] have shown that the corresponding $\gamma\gamma \to$ pseudoscalar and tensor meson channels can be used to isolate the Odderon exchange contribution, that is contributions related at a fundamental level to three gluon exchange.

16. Heavy Quark Pair Production in $\gamma\gamma$ Collisions

The leading contributions to heavy quark production in $\gamma\gamma$ collisions are illustrated in Fig. 26. The resolved contributions depend in detail on the assumed form of the photon's gluon distribution.

The cross section for direct heavy quark production $\sigma \sim \pi\alpha^2/m_Q^2$ is of order 130 nb and 1300 pb for $c\bar{c}$ and $b\bar{b}$ production, respectively. The top pair cross section $\sigma_{t\bar{t}}$ is of order of $\frac{1}{2}\,\sigma_{e^+e^-\to\mu^+\mu^-}$ at the corresponding energy [11,101,102]. Figure 27 shows the prediction of Drees, Krämer, Zunft and Zerwas [103] for the inclusive charm production cross sections in $e^+e^- \to e^+e^- q\bar{q}X$ using the equivalent photon approximation. The vertical bars on the left represent the estimated uncertainty due to the scale dependence of the lowest order of predictions. The bar on the right shows the dependence on the quark mass. TPC$\gamma\gamma$ and TRISTAN data for $\sigma(e^+e^- \to\to D^{*\pm}X)$ are compared with the QCD prediction of Drees *et al.* in Fig. 28.

Figure 29 a shows the cross section predicted by Kühn, Mirkes and Steegborn [104] for $t\bar{t}$ production including higher order QCD corrections. The predicted rate is given for $m_t = 150$ GeV as a function of the center mass energy of the e^+e^- collider, where a convolution with the computed photon energy spectrum of the back-scattered laser beam is assumed. Since the top mass is greater than 120 GeV, its decay width due to weak decays $\Gamma = 2\Gamma(t \to bW)$ is so large that true bound states $t\bar{t}$ cannot form; nevertheless there can be significant threshold effects [105,106]. As shown in Fig. 29b, if the experiment resolution in $\mathcal{M}_{t\bar{t}}$ is sufficient, then it may be possible to resolve the predicted structure of the $\gamma\gamma \to t\bar{t}$ cross section near the top threshold. Detailed predictions for this threshold dependence as a function of the top quark mass have been given by Bigi, Gabbiani, and Khoze [107]. The combination of $\gamma\gamma$ ($C = +$)and e^+e^- ($C = -$) measurements of the $t\bar{t}$ threshold spectrum could provide a very precise value for the top quark mass.

17. Single Top Quark Production

A single top quark can be produced in electron-photon collisions at an NLC through the process $e^-\gamma \to W^-t\nu$ [108,28]. This process can be identified through the $t \to W^+b$ decay with $W \to \ell\overline{\nu}$. The rate is thus sensitive to the V_{tb} matrix element and possible fourth generation quarks and anomalous couplings. An interesting background is the virtual W process $e\gamma \to W^* - \nu \to W^-H\nu$, where the Higgs boson decays to $b\bar{b}$ and $W^- \to \ell\overline{\nu}$. The rates for the signal and background processes as a function of $\sqrt{s}_{e^+e^-}$ computed by Cheung [28] and Yehudai [24] are shown in Fig. 30.

18. Higgs Plus Top Quark Pair Production

The tree process $\gamma\gamma \to t\bar{t} + H$ can provide a direct measure of coupling of the Higgs boson to heavy quarks. The cross section has been estimated by Boos [54] and Cheung [28] to be of order 1 to 5 fb. Cheung [28] has also computed the radiative corrections to $\gamma\gamma t\bar{t}$ from final state Higgs exchange interactions. The correction is of $\mathcal{O}(2-4\%)$ for typical values of the Higgs boson mass and top quark mass.

19. Conclusions

Photon-photon collisions at a linear e^+e^- collider in the TeV range will provide an extraordinary window for testing electroweak and QCD phenomena as well as proposed extensions of the Standard Model, such as supersymmetry [109], technicolor, and other composite models. Two-photon physics is unique in that virtually all charged particles and their bound states and resonances with positive C can be produced; in addition one can access pairs of fundamental neutral particles through one-loop corrections. It will be essential to have the capability of back-scattered

laser beams at the NLC, since it is expected that the resulting luminosity and effective energy of photon-photon and photon-electron collisions will be comparable to that of the primary e^+e^- collisions. Such a facility, together with polarized electron beams, will also allow the study of the physics of highly-polarized photon-photon and electron-photon collisions. There is also a wide range of physics topics which could be addressed in polarized electron-electron collisions, if such a capability were available [110].

Two-photon physics is an extensive phenomenological field, having elements in common with both e^+e^- and hadron-hadron collisions. However, the combination of direct photon and resolved processes gives $\gamma\gamma$ physics an extra dimension in probing new phenomena. For example, since each photon can be resolved into a W^+W^- pair, high energy photon-photon collisions can provide a remarkably background-free laboratory for studying WW collisions and annihilation. Thus a photon-photon collider can also become the equivalent a WW collider to study whether the interactions of longitudinally polarized W's are controlled by Higgs annihilation and exchange or a new type of strong interaction.

It is clear that $\gamma\gamma$ collisions are an integral part of the NLC physics program. It was possible to highlight only a small part of the possible new $\gamma\gamma$ physics topics here. At present energies, studies of $\gamma\gamma$ collisions at CESR, PETRA, PEP, TRISTAN, and LEP have led to a number of important tests of perturbative and non-perturbative QCD in exclusive and inclusive reactions, heavy quark phenomena, and resonance formation. Reviews of the results of these experiments and the underlying theory of $\gamma\gamma$ collisions are given in Refs. [7], [12], [16], [17], [19], [20] and the proceedings of the International Workshops on Photon-Photon collisions.

Acknowledgements

This work was supported in part by Deutsche Forschungsgemeinschaft DFG. Part

of this work was also presented at the Second International Workshop on Physics and Experiments with Linear Colliders, Waikoloa, Hawaii. The review of the photon structure function given here is based on work done in collaboration with Michael Krämer. SJB also thanks David Borden, Michael Boulware, George Jikia, and Ilya Ginzburg for helpful conversations.

Appendix I: The Photon's Light-Cone Fock Expansion

One can distinguish the various contributions to the photon's direct and resolved interactions in the following way: Consider the Lagrangian for the Standard Model cutoff at an ultraviolet scale Λ and the corresponding light-cone time $\tau = t - z/c$ evolution operator; *i.e.*, the light-cone Hamiltonian $H_{LC}^{(\Lambda)}$. The photon is the physical zero-mass eigenstate of the full Hamiltonian. Any eigenstate of the full Hamiltonian can be expanded as a sum of eigenstates of the free Hamiltonian: $|\psi\rangle = \sum_n |n\rangle \langle n | \psi\rangle$. The photon state is thus equivalent to a coherent sum of free Fock states with the same charge and color singlet quantum numbers. The coefficients in this expansion, $\langle n | \psi\rangle = \psi_{n/\gamma}^{(\Lambda)}(x_i, \vec{k}_{\perp i}, \lambda_i)$, with $\sum x_i = 1$ and $\sum \vec{k}_{\perp i} = 0$ are the basic wavefunction matrix elements needed to describe the photon in terms of its quark and gluon and other Standard Model degrees of freedom. The $\psi_{n/\gamma}^{(\Lambda)}(x_i, \vec{k}_{\perp i}, \lambda_i)$, are frame independent functions of the light-cone fractions $x_i = k_i^+/p^+$, the relative transverse momenta $k_{\perp i}$, and the spin projections λ_i [10]. Since the photon is an elementary field, the physical photon has a non-zero bare component in the Fock expansion: $\psi_\gamma^0(x, k_\perp) = 16\pi^3 \sqrt{Z_3(\Lambda^2)} \delta(1-x)\, \delta^2(\vec{k}_\perp)\, \delta_{\lambda\lambda'}$ where $Z_3(\Lambda^2)$ is the probability that the photon stays a bare photon at the cutoff scale Λ.

Given the photon's Fock expansion we can calculate the photon- photon scattering amplitude at high momentum transfer in terms of its constituents' interactions in the

factorized form shown in Fig. 1 and

$$\mathcal{M} = \sum_{n,m} \int \frac{\overline{\pi} d^2 k_\perp dx}{16\pi^3} \psi_n^{(\Lambda)}(x_i, k_{\perp i} \lambda_i) \int \frac{\overline{\pi} d^2 \ell_\perp dy}{16\pi^3} \psi_m^{(\Lambda)}(y_i, \ell_{\perp i}, \lambda_i) T_{ab\to cd}^{(\Lambda)} \cdot$$

Here $T_{ab\to cd}^{(\Lambda)}$ is a sum over all $2 \to 2$ and higher subprocess amplitudes. It is irreducible and contains all the interactions, radiative corrections, and loop corrections with $k_\perp^2$ greater than the separation scale Λ^2. Higher particle processes are generally higher twist and thus power-law suppressed at large momentum transfer. In the expansion of the $\gamma\gamma$ scattering amplitude one thus obtains the direct pair production processes from the bare photon components as well as the resolved contributions. One can then square the matrix element, integrate over undetected variables, and derive the usual factorized form for hard scattering processes in QCD, but with the special addition of contributions from the direct-direct and direct-resolved $\gamma\gamma$ processes.

Appendix II. The Photon-Hadron Coherence Length

At very high energies the hadronic component of a photon state resembles a coherent sum of vector mesons. The coherence time, as discussed by Ioffe [2] and by Yennie *et al.* [3], is $\Delta\tau = \frac{1}{\Delta E} = \frac{2P_\gamma^+}{Q^2+\mathcal{M}^2}$ for intermediate vector states of mass $\mathcal{M}$. Thus in high energies photon-nucleus reactions, a real or virtual photon will generally convert to a hadronic system well before interacting in the target, and the energy and nuclear size dependence of the photon-induced cross sections will resemble that of meson-induced reactions. In fact, as shown in Ref. [111], the coherence time of a virtual photon depends on whether its polarization is longitudinal or transverse: $\tau_L = \tau_T/\sqrt{3}$. Thus shadowing of the nuclear photoabsorption cross section will be delayed to higher energies in the case of longitudinal current–nuclear interactions.

The long coherence length between photons and the intermediate vector states at high energies and the resulting photon-hadron duality can be used as a general guide

to the hadronic interactions of photons at low transverse momentum. In particular the long coherence length implies pomeron factorization of photon-induced cross sections [6]: $\sigma_{\gamma\gamma} = \frac{\sigma^2_{\gamma p}}{\sigma_{pp}}$ Thus one should be able to track the slow increase of the total inelastic photon-photon cross section with that of the γp and pp cross section.

20. Figure Captions

Figure 1:

Factorization of the resolved photon-photon amplitudes using the light-cone Fock basis. (See Appendix I.) In the case of the direct contributions, the photon annihilates within the hard scattering amplitude.

Figure 2:

The $\gamma\gamma$ luminosity in Compton back–scattering of laser light; unpolarized $e^{\pm}$ beams and laser photons (dashed), opposite helicities of $e^{\pm}$ and γ (full curve). See Refs. [45], [50], [104].

Figure 3:

(a) Degree of circular polarization of the high energy photons in polarized Compton back–scattering of laser light for different $e^{\pm}$ and γ helicity modes. (b) Left/right asymmetry of the final state photon beam in Compton back–scattering of laser light. (c) Spectrum and degree of linear polarization of the high-energy photons in Compton back–scattering of linearly polarized laser light; Ref. [48].

Figure 4:

Illustration of direct, resolved, and higher-order loop contributions to high energy $\gamma\gamma$ collisions.

Figure 5:

Representative cross sections for W^+W^-production and other electroweak reactions at a $\gamma\gamma$ and e^+e^- linear collider. The top mass is taken as 130 GeV. The other

subscripts refer to the mass of the Higgs (in GeV). The Higgs mass is set to zero for the reactions $e^+e^- \to W^+W^-\nu\bar{\nu}$ and $e^+e^- \to ZZ\nu\bar{\nu}$. From Refs. [27,63,22].

Figure 6:

Differential cross sections for producing a W pair of a specific helicity combination at $\sqrt{s}_{\gamma\gamma} = 500$ GeV as a function of $\cos\theta$. The curves are:

1: (++++)+(—), 2: (+++-)+(++-+)+(-+-)+(—+),

3: (++–)+(-++), 4: (+-++)+(-+++)+(+—)+(-+-),

5: (+-+-)+(-+-+)+(-++-)+(+–+),

6: (+-+-)+(-+0-)+(+–0)+(-++0)+(+-+0)+(-+-0)+(+-0-)+(-+0+),

7: (+-00)+(-+00), 8: (++0+)+(–0-)+(+++0)+(—0),

9: (++00)+(–00), 10: (++0-)+(++-0)+(–0+)+(–+0).

The notation indicates $(\lambda_1\lambda_2\lambda_3\lambda_4)$, where $\lambda_1, \lambda_2, \lambda_3$ and λ_4 are the helicities of the two photons and the W^+ and the W^- respectively. From Ref. [24].

Figure 7:

Standard Model one-loop contributions to the reaction $\gamma\gamma \to ZZ$ including ghost $c^{\pm}$ and scalar w contributions in the background nonlinear gauge. From Ref. [41].

Figure 8:

The effective cross section for $\gamma\gamma \to Z^0\gamma$ at an NLC taking into account the back-scattered laser spectrum. The fermion and W loop contributions are shown for the production of a transversely (T) and longitudinally (L) polarized Z^0. The incident photons are taken to have positive helicity. From Ref. [41].

Figure 9:

Number of events per year for the Standard Model Higgs boson ($\Phi^0 \to b\bar{b}, t\bar{t}, ZZ$) and for the heavy–quark backgrounds; Ref. [46]. Here $\mathcal{L}_{\rm eff} = 20\, fb^{-1}$, $z_0 = 0.85$, $\langle\lambda_1\lambda_2\rangle = 0.8$, $\Gamma_{\rm expt} = 5\ GeV$.

Figure 10:

Expected event rates for the Higgs signal and the background processes in $b\bar{b}, c\bar{c}$ two–

jet final states for polarized γ beams; Ref. [58].

Figure 11:

Invariant mass distribution in $\gamma\gamma \to H \to ZZ$ and in the continuum $\gamma\gamma \to ZZ$ for transverse and longitudinal Z polarization; Ref. [41].

Figure 12:

The $\gamma\gamma$ polarization asymmetry $\mathcal{A}$ in Compton back–scattering of linearly polarized laser light for various values of x_0; Ref. [48].

Figure 13:

$\mathcal{MSSM}$ Higgs particle h^0: signal and background cross sections for $b\bar{b}$ final states (a), and the polarization asymmetry $\mathcal{A}(h^0)$ including the background process (b); Ref. [48].

Figure 14:

$\mathcal{MSSM}$ Higgs particle A^0: signal and background cross sections for $b\bar{b}$ final states (a), and the polarization asymmetry $\mathcal{A}(A^0)$ including the background process (b); Ref. [48].

Figure 15:

Illustration of WW scattering at a photon-photon collider. The kinematics of the interacting W's can be determined by tagging the spectator W's. The interacting pair can scatter or annihilate, for example into a Higgs boson.

Figure 16:

(a) Deep-inelastic electron-photon scattering $e\gamma \to eX$.

(b) The charged current process $e\gamma \to \nu X$ in deep–inelastic $e\gamma$ scattering.

Figure 17:

Event plane $\mathcal{P} = [\log Q^2, \log(1/x - 1)]$ in $e\gamma$ scattering (Q^2 is defined in GeV^2). Shown are the two parallelograms which can be explored at LEP200 and LC500 and within which perturbative QCD can be applied.

Figure 18:

QCD prediction for the photon structure $F_2^\gamma(x, Q^2)$ at $Q^2 = 200$ GeV^2 and sensitivity to the QCD Λ parameter. Error bars correspond to an integrated luminosity of 500 pb^{-1} at LEP200 and the range $100 < Q^2 < 500$ GeV^2. From Ref. [85].

Figure 19:

Comparison of the Q^2 evolution of the photon structure function in QCD with a model in which the coupling constant is frozen.

Figure 20:

Experimentally observed Q^2 evolution of the photon structure function; from Ref. [79].

Figure 21:

Comparison of perturbative QCD predictions with PLUTO data for the photon structure function at $Q^2 = 5.9$ GeV^2. The charm quark contribution from leading and higher order QCD is also shown. From Ref. [81].

Figure 22:

Theoretical estimate of the sensitivity to the effective QCD scale parameter, (a) from the evolution of F_2^γ at large x; (b) from the absolute size of F_2^γ if the hadronic component is assumed to be uncertain within $\pm 50\%$ at $Q^2 = 100$ GeV^2.

Figure 23:

QCD contributions to jet transverse momentum cross section in $\gamma\gamma$ collisions. The resolved contributions are based on the Drees-Godpole model for the gluon distribution in the photon. From Ref. [11].

Figure 24:

The effect of multiple scattering on the mini-jet contribution to the $\gamma\gamma$ total cross section. The jet contributions are shown for various p_T minimum cut-offs, with (solid line) and without (dashed line) the effect of eikonalization. From Ref. [96].

Figure 25:

Perturbative QCD contributions to large momentum transfer exclusive double diffrac-

tive $\gamma\gamma$ processes. The two-gluon exchange pomeron contributions to vector meson pair production and three-gluon exchange odderon contributions to neutral pseudoscalar and tensor meson pair production are illustrated.

Figure 26:

Direct and resolved contributions to heavy quark production in $\gamma\gamma$ collisions.

Figure 27:

QCD leading and next-to-leading order contributions to the inclusive charm production cross section. The resolved contributions are based on the Drees-Godpole model for the gluon distribution in the photon. From Ref. [103].

Figure 28:

TPC$\gamma\gamma$, TASSO, and TRISTAN data for $\sigma(e^+e^- \to e^+e^- D^{*\pm} X)$ compared with the QCD prediction of Drees *et al.* From Ref. [103]. The dashed lines show the once-resolved contributions. The upper line is $\mu = m_c = 1.3$ GeV. The lower line is $\mu = 2m_c$, $m_c = 1.8$ GeV.

Figure 29:

(a) Effective cross section $\langle \sigma(\gamma\gamma \to t\bar{t}) \rangle / \sigma(e^+e^-)_{pt}$ with (solid) and without (dashed) QCD corrections for $m_t = 150$ *GeV*. The convolution with a back-scattered laser spectrum ($\omega = 1.26$ eV) is included. (b) The effective differential cross section $d\langle \sigma(\gamma\gamma \to t\bar{t}) \rangle / dz / \sigma(e^+e^-)_{pt}$ and the resonance signal predicted at $\sqrt{s_{e^+e^-}} = 500$ GeV. Here $z = \mathcal{M}_{t\bar{t}}/\sqrt{s_{e^+e^-}}$. From Ref. [104].

Figure 30:

The single top production cross section and its competing backgrounds in high energy electron-photon collisions. From Ref. [28].

21. References

[1] The Fock state decomposition of the photon and a description of photon-photon collision processes at the amplitude level are discussed in Appendix I.

[2] B. L. Ioffe, *Phys. Lett.* **30B** (1969) 123; J. Pestieau, P. Roy, and H. Terazawa, *Phys. Rev. Lett.* **25** (1970) 402; A. Suri and D. R. Yennie, *Ann. Phys. (N.Y.)* **72** (1972) 243. See also, L. Stodolsky, in the *Proceedings of the International School of Elementary Particle Physics*, Herceg-Novi, Yugoslavia, (1969). Edited by M. Nikolic. N.Y., Gordon and Breach, 1977.

[3] T. H. Bauer, R. D. Spital, and D. R. Yennie, *Rev. Mod. Phys.* **50** (1968) 261.

[4] For further discussion of the photon formation time, see Appendix II.

[5] For a recent review of the hadronic aspects of photon-photon collisions, see G. A. Schuler and T. Sjöstrand, CERN-TH-7193-04, presented at Two-Photon Physics from DAPHNE to LEP200 and Beyond, Paris, France, 2-4 Feb 1994. (1994).

[6] S. J. Brodsky, T. Kinoshita, and H. Terazawa, *Phys. Rev. Lett.* **25** (1970) 972; *Phys. Rev.* **D4** (1971) 1532.

[7] For a review of additional aspects of hadronic $\gamma\gamma$ physics and further references, see P. Kessler, *Proceedings of the IXth International Workshop on Photon-Photon Collisions*, D. Caldwell and H. Paar, eds. (World Scientific, 1992.)

[8] T. F. Walsh, *Phys. Lett.* **36B** (1971) 121.

[9] E. Witten, *Nucl. Phys.* **B120** (1977) 189.

[10] G. P. Lepage and S. J. Brodsky, *Phys. Rev.* **D22** (1980) 2157. S. J. Brodsky and G. P. Lepage, *Phys. Rev.* **D24** (1981) 1808; **D24** (1981) 2848.

[11] S. J. Brodsky, T. DeGrand, J. Gunion, and J. Weis, *Phys. Rev. Lett.* **41** (1978) 672; *Phys. Rev.* **19,** (1979) 1418. The descriptive terms, direct and resolved, were introduced by M. Drees and R. M. Godpole, these proceedings, *Nucl.*

Phys. **B339** (1990) 355; *Phys. Rev. Lett.* **67** (1992) 1189; and DESY 92-044 (1992). M. Drees, DESY 92-065 (1992).

[12] For a review of two-photon exclusive processes, see S. J. Brodsky, *Proceedings of the IXth International Workshop on Photon-Photon Collisions,* D. Caldwell and H. Paar, eds. (World Scientific, 1992.)

[13] T. Hyer, *Phys. Rev.* **D47** (1993) 3875.

[14] See I. F. Ginzburg, *Proceedings of the Second International Workshop on Physics and Experiments with Linear Colliders,* Waikoloa, Hawaii (1993), Ed. F. A. Harris *et al.*, World Scientific. and the *Proceedings of the IXth International Workshop on Photon-Photon Collisions,* D. Caldwell and H. Paar, eds. (World Scientific, 1992.)

[15] The production of non-strongly interacting supersymmetric particles in $\gamma\gamma$ collisions is discussed by J. Ohnemus, T. F. Walsh, and P. M. Zerwas, DESY 93-173 (1993).

[16] H. Kolanoski and P. Zerwas, DESY 87-185 (1987), published in "High Energy Electron-Positron Physics,", eds. A. Ali and P. Söding, World Scientific, Singapore.

[17] J. H. Field, preprint L.P.N.H.E. 84-04 (1984).

[18] Ch. Berger and W. Wagner, *Phys. Rep.* **136** (1987) 1.

[19] H. Kolanoski, Two-Photon Physics at e^+e^- Storage Rings, Springer Verlag, 1984)

[20] S. J. Brodsky, in the *Proceedings of the IXth International Workshop on Photon-Photon Collisions*, Shoresh, Israel (1988).

[21] D. L. Borden, D. A, Bauer, D. O. Caldwell, SLAC-PUB-5715 (1992).

[22] For a comprehensive review of electroweak physics at a high energy $\gamma\gamma$ collider, see M. Baillargeon, G. Belanger, and F. Boudjema, ENSLAPP-A-473 (1994).

[23] For a review of the $\gamma\gamma \to WW$ process, and further references see M. Baillargeon and F. Boudjema, *Phys. Lett.* **B288** (1992) 210.

[24] E. Yehudai, *Proceedings of the Second International Workshop on Physics and Experiments with Linear Colliders*, Waikoloa, Hawaii, (1993), Ed. F. A. Harris *et al.*, World Scientific; SLAC-383 (1991); *Phys. Rev.* **D44** (1991) 3434; *Phys. Rev.* **D41** (1990) 33.

[25] S. J. Brodsky, *Proceedings of the Second International Workshop on Physics and Experiments with Linear Colliders*, Waikoloa, Hawaii,(1993), Ed. F. A. Harris *et al.*, World Scientific, Vol I, p. 295.

[26] S. J. Brodsky, and G. Jikia, in progress.

[27] G. Jikia , these proceedings; and Protovino preprint (1994), hep-ph/9406395.

[28] K. Cheung, *Proceedings of the Second International Workshop on Physics and Experiments with Linear Colliders*, Waikoloa, Hawaii (1993), Ed. F. A. Harris *et al.*, World Scientific. Northwestern preprint NUHEP-TH-93-3, (1993). See also K. Cheung, *Phys. Rev.* **D47** (1993) 3750. D. Bowser-Chao, K. Cheung, and S. Thomas, Northwestern preprint NUHEP-TH-93-7 (1993).

[29] K. Cheung, *Phys. Lett.* **B323** (1994) 85, Northwestern preprint NUHEP-TH-94-13 (1994), and these proceedings.

[30] I. Ginzburg, G. Kotkin, V. Serbo, and V. Telnov, *JETP Lett.* **34** (1982) 491. For further references and reviews see the contributions of V. Telnov, V. Balakin and I. F. Ginzburg, and D. Borden, *Proceedings of the Second International Workshop on Physics and Experiments with Linear Colliders*, Waikoloa, Hawaii, (1993), Ed. F. A. Harris *et al.*, World Scientific, and the reports of V. Telnov and J. Spencer in the *Proceedings of the IXth International Workshop on Photon-Photon Collisions*, D. Caldwell and H. Paar, eds. (World Scientific, 1992.)

[31] The spectrum of beamstrahlung photons depends on the machine design; see T. Barklow, P. Chen, and W. Kozanecki, SLAC-PUB 5718 (1992) and Proceedings "e^+e^- Collisions at 500 GeV: The Physics Potential", Munich–Annecy–Hamburg 1991, DESY 92-123B.

[32] R. Blankenbecler and S. D. Drell, *Phys. Rev. Lett.* **61** (1988) 2324; *Phys. Rev.* **D37** (1988) 3308; *Phys. Rev.* **D36** (1987) 277.

[33] M. Jacob and T. T. Wu, in the *Proceedings of the Lepton/Photon Symposium* (1991); *Phys. Lett.* **B216** (1989) 442; *Phys. Lett.* **197B** (1987) 253.

[34] D. Miller, *Proceedings of the Second International Workshop on Physics and Experiments with Linear Colliders*, Waikoloa, Hawaii, (1993), Ed. F. A. Harris *et al.*, World Scientific.

[35] G. Jikia and A. Tkabladze, *Phys. Lett.* **B323** (1994) 453.

[36] A. Djouadi, M. Spira, and P. M. Zerwas, DESY 92-170. K. Melnikov and O. Yakovlev, Novosibirsk BUDKERINP preprint 93-4 (1993).

[37] S. D. Drell and A. C. Hearn, *Phys. Rev. Lett.* **16** (1966) 908; S. B. Gerasimov. *Yad. Fiz* **2** (1965) 598 [*Sov. J. Nucl. Phys.* **2** (1966) 430]; M. Hosoda and K. Yamamoto, *Prog. Theor. Phys.* **36** (1966) 426; see also S. J. Brodsky and J. R. Primack, *Ann. Phys. (N.Y.)* **52** (1960) 315.

[38] S. J. Brodsky and J. R. Hiller, *Phys. Rev.* **D46** (1992) 2141.

[39] W.- K. Tung, *Phys. Rev.* **176** (1968) 2127.

[40] S. J. Brodsky and S. D. Drell, *Phys. Rev.* **D22** (1980) 2236.

[41] *Nucl. Phys.***B405** (1993) 24; *Phys. Lett.* **B298** (1993) 224. See also G. Jikia, these proceedings; the *Proceedings of the Second International Workshop on Physics and Experiments with Linear Colliders*, Waikoloa, Hawaii (1993), Ed. F. A. Harris *et al.*, World Scientific; and Protvino preprints IHEP 92-91 (1992), 93-37 (1993). E. E. Boos and G.V. Jikia *Phys. Lett.* **B275** (1992) 164.

[42] F. E. Low, *Phys. Rev.* **120** (1960) 582.

[43] H. Aihara *et al.*, *Phys. Rev. Lett.* **60** (1988) 2355.

[44] For a review see J. F. Gunion, H. E. Haber, G. L. Kane and S. Dawson, "The Higgs Hunter's Guide", Addison-Wesley 1990.

[45] D. L. Borden, D. A. Bauer and D. O. Caldwell, SLAC-PUB-5715 and *Phys. Rev.* **D48** (1993) 4018.

[46] J. F. Gunion and H. E. Haber, *Phys. Rev.* **D48** (1993) 5109.

[47] B. Grzadkowski and J.F. Gunion, *Phys. Lett.* **B294** (1992) 361.

[48] M. Krämer, J. Kühn, M. L. Stong and P. M. Zerwas, DESY 93-174 [*Z. Phys. C in print*].

[49] J. F. Gunion and J. G. Kelly, Preprint UCD-94-20.

[50] I. F. Ginzburg, G. L. Kotkin, S. L. Panfil, V. G. Serbo and V. I. Telnov, *Nucl. Instr. and Meth.* **219** (1984) 5.

[51] Wai-Keung Tang, to be published.

[52] For a review see P.M. Zerwas (*ed.*), "e^+e^- Collisions at 500 GeV: The Physics Potential", DESY 92-123A+B and 93-123C.

[53] D. L. Borden, D. A. Bauer, and D. O. Caldwell, UCSB-HEP 93-01 (1993).

[54] E. Boos, *Proceedings of the Second International Workshop on Physics and Experiments with Linear Colliders*, Waikoloa, Hawaii (1993), Ed. F. A. Harris *et al.*, World Scientific, and E. Boos, I. Ginzburg, K. Melnikov, T. Sack, and S. Shichanin, *Z. Phys.* **56** (1992) 487.

[55] J. Ellis, M. K. Gaillard and D. V. Nanopoulos, *Nucl. Phys.* **B106** (1976) 292; A. Djouadi, M. Spira, J. J. van der Bij and P. M. Zerwas, *Phys. Lett.* **B257** (1991) 187; M. Spira, Thesis, RWTH Aachen 1992; K. Melnikov and O. Yakovlev, *Phys. Lett.* **B312** (1993) 179.

[56] H. Veltman, *Z. Phys.* **C62** (1994) 235.

[57] M. Drees, M. Krämer, J. Zunft and P. M. Zerwas, *Phys. Lett.* **B306** (1993) 371.

[58] G. Jikia and A. Tkabladze, IHEP–Protvino Preprint 1994.

[59] D. L. Borden, V. A. Khoze, W. J. Stirling and J. Ohnemus, Preprint UCD–94–8.

[60] M. S. Berger, *Phys. Rev.* **D48** (1993) 5121; D. A. Dicus and C. Kao, *Phys. Rev.* **D49** (1994) 1265.

[61] A. Djouadi, M. Spira and P. M. Zerwas, *Phys. Lett.* **B311** (1993) 255; K. Melnikov, M. Spira and O. Yakovlev, DESY 94–076 *[Z. Phys. C. in print].*

[62] Higgs production in electron-photon collisions is discussed by K. Hagiwara I. Watanabe, and P. M. Zerwas, *Phys. Lett.* **B278** (1992) 187.

[63] M. Baillargeon and F. Boudjema, *Phys. Lett.* **B317** (1993) 371. See also M. Baillargeon and F. Boudjema, ENSLAPP-A-400-92, Aug 1992, published in the *Proceedings of the conference Beyond the Standard Model III*, Ottawa, Canada, (1992) 387.

[64] This section was prepared in collaboration with M. Krämer.

[65] T. F. Walsh and P. M. Zerwas, *Phys. Lett.* **B44** (1973) 196.

[66] S. J. Brodsky, T. Kinoshita, and H. Terazawa, *Phys. Rev. Lett.* **27** (1971) 280.

[67] Ch. Berger and W. Wagner, *Phys. Rep.* **C146** (1987) 1.

[68] For a summary see J. Storrow, *Proceedings, "Two–Photon Physics at LEP and HERA"*, Lund 1994; and M. Fontannaz, *ibid.*

[69] G. Schuler and T. Sjöstrand, *Nucl. Phys.* **B407** (1993) 539 and *Proceedings, "Two–Photon Physics from Daphne to LEP200 and Beyond"*, Paris 1994.

[70] R. J. DeWitt, L. M. Jones, J. D. Sullivan, D. E. Willen, H. W. Wyld, Jr., *Phys. Rev.* **D19** (1979) 2046.

[71] D. Miller, *Proceedings, "ECFA Workshop on LEP200"*, Aachen 1986, CERN 87-08, and *Proceedings, "Lepton–Photon Symposium"*, Cornell 1993.

[72] W. A. Bardeen and A. J. Buras, *Phys. Rev.* **D20** (1979) 166; D21 (1980) 2041 (E); M. Fontannaz and E. Pilon, *Phys. Rev.* **D45** (1992) 382; M. Glück, E. Reya and A. Vogt, *Phys. Rev.* **D45** (1992) 3986.

[73] G. Rossi, *Phys. Lett.* **B130** (1983) 105.

[74] I. Antoniades and G. Grunberg, *Nucl. Phys.* **B213** (1983) 445.

[75] For a recent discussion of various schemes for the higher corrections, including numerical analyses, see A. Vogt, *Proceedings, "Two-Photon Physics at LEP and HERA"*, Lund 1994.

[76] In higher orders, for instance in the renormalization scheme $\overline{MS}$, $\Lambda^{(N_F)}_{\overline{MS}}$ carries the index of the active flavors. Since the data with the smallest errors had been collected in the past for Q^2 values of $\mathcal{O}(10\ \mathrm{GeV}^2)$, early experimental analyses [67] correspond to $\Lambda^{(4)}_{\overline{MS}}$ with four flavor degrees of freedom.

[77] C. Peterson, T. F. Walsh and P. M. Zerwas, *Nucl. Phys.* **B299** (1983) 301.

[78] For off-shell γ targets, $\Lambda^2 \ll P^2 \ll Q^2$, the gluon radiation is reduced, and the structure function approaches the Born term again with increasing P^2. See also T. Uematsu and T. F. Walsh, *Phys. Lett.* **B101** (1981) 263.

[79] T. Sasaki et al., *Phys. Lett.* **B252** (1990) 491.

[80] E. Witten, *Nucl. Phys.* **B104** (1976) 445; C. T. Hill and G. G. Ross, *Nucl. Phys.* **B148** (1979) 373; M. Glück and E. Reya, *Phys. Lett.* **B83** (1979) 98.

[81] E. Laenen, S. Riemersma, J. Smith and W.L. van Neerven, Fermilab–Pub–93/240–T.

[82] We give only crude estimates in this section for effective values of α_s and Λ; the analysis must necessarily be refined by including higher orders to define α_s properly. See Ref. [75]. Alternatively, the $\overline{MS}$ scheme and scale dependence of the photon structure functions can be eliminated in terms of an effective charge defined from a physical observable. See S. J. Brodsky and H. J. Lu,

SLAC–PUB–6481 (1994).

[83] J. D. Bjorken, SLAC–PUB–5103.

[84] W. Ibes and T. F. Walsh, *Phys. Lett.* **B251** (1990) 450; S. M. Kim and T. F. Walsh, Minnesota Preprint UMN–TH–1111/92.

[85] See A. Cordier et al, LEP200 Workshop, CERN 87-08 (1987).

[86] A. C. Bawa and M. Krawczyk and W. J. Stirling *Z. Phys.* **C50** (1991) 293; A. C. Bawa and M. Krawczyk, *Phys. Lett.* **B262** (1991) 492.

[87] E. A. Kuraev, L. N. Lipatov and V. S. Fadin, Sov. Phys. JETP 45 (1977) 199; Ya. Ya. Balitzkij and L. N. Lipatov, Sov. J. Nucl. Phys. 28 (1978) 822.

[88] J. R. Forshaw and P. N. Harriman, *Phys. Rev.* **D46** (1992) 3778.

[89] I.F. Ginzburg, G.L. Kotkin, V.G. Serbo and V.I. Telnov, *Nucl. Instr. and Meth.* **219** (1984) 5.

[90] C. Peterson, T. F. Walsh and P. M. Zerwas, *Nucl. Phys.* **B174** (1980) 424.

[91] G. Altarelli and G. Martinelli, *Phys. Lett.* **B76** (1978) 89.

[92] A. V. Efremov and O. V. Teryaev, *Phys. Lett.* **B240** (1990) 200; S. D. Bass, Int. J. Mod. Phys. A7 (1992) 6039; S. Narison, G. M. Shore and G. Veneziano, *Nucl. Phys.* **B391** (1993) 69; G. M. Shore and G. Veneziano, Mod. Phys. Lett. A8 (1993) 373.

[93] C. H. Llewellyn Smith, *Phys. Lett.* **B79** (1979) 83.

[94] T. Tauchi,*et al.*, *Proceedings of the Second International Workshop on Physics and Experiments with Linear Colliders*, Waikoloa, Hawaii, (1993), Ed. F. A. Harris *et al.*, World Scientific. H. Hayashii, *et al.*, KEK-Preprint-93-47, (1993).

[95] H. Abromowicz, K. Charchula, and A. Levy, *Phys. Lett.* **B269** (1991) 458. A. Levy, *Proceedings of the IXth International Workshop on Photon-Photon Collisions*, D. Caldwell and H. Paar, eds. (World Scientific, 1992.)

[96] J. K. Storrow, *Proceedings of the Second International Workshop on Physics and Experiments with Linear Colliders*, Waikoloa, Hawaii, (1993), Ed. F. A. Harris *et al.*, World Scientific. J. R. Forshaw and J. K. Storrow, *Proceedings of the IXth International Workshop on Photon-Photon Collisions*, D. Caldwell and H. Paar, eds. (World Scientific, 1992.); *Phys. Rev.* **D46** (1992) 4955.

[97] P. Chen, *Proceedings of the Second International Workshop on Physics and Experiments with Linear Colliders*, Waikoloa, Hawaii, (1993); Ed. F. A. Harris *et al.*, World Scientific. P. Chen, T. L. Barklow, M. E. Peskin, *Phys. Rev.* **D49** (1994) 3209.

[98] I. Ginzburg, *Proceedings of the Second International Workshop on Physics and Experiments with Linear Colliders*, Waikoloa, Hawaii, (1993), Ed. F. A. Harris *et al.*, World Scientific.

[99] I. F. Ginzburg and D. Yu. Ivanov, *Nucl. Phys.* **B388** (1992) 376.

[100] V. L. Chernyak and I. R. Zhitnitsky, *Phys. Rep.* **112** (1984) 1783. Novosibirsk Inst. Nucl. Phys. Acad. Sci. preprint 82-44 (1982).

[101] O. J. P. Eboli, M. C. Gonzalez-Garcia, F. Halzen, and S. F. Novaes, *Phys. Rev.* **D47** (1993) 1889 and *Phys. Lett.* **B301** (1993) 115.

[102] O. J. P. Eboli, M. C. Gonzalez-Garcia, F. Halzen, and D. Zeppenfeld, *Phys.Rev.* **D48** (1993) 224. See also F. Ginzburg and V. G. Serbo, *Proceedings of the Second International Workshop on Physics and Experiments with Linear Colliders*, Waikoloa, Hawaii (1993), Ed. F. A. Harris *et al.*, World Scientific.

[103] M. Drees, M. Krämer, J. Zunft, and P. M. Zerwas, DESY 92-169 (1992).

[104] J. H. Kühn, E. Mirkes, and J. Steegborn, Karlsruhe preprint TTP92-28 (1992). Z. Phys. C57 (1993) 615.

[105] J. H. Kühn and P. M. Zerwas, *Phys. Rept.* **167** (1988) 321.

[106] S. J. Brodsky, G. Köpp, and P. M. Zerwas, *Phys. Rev. Lett.* **58** (1987) 443.

[107] I. L. Bigi, F. Gabbiani, and V. A. Khoze, SLAC-PUB 5951 (1992).

[108] G. V. Jikia, *Nucl. Phys.* **B374** (1992) 83.

[109] F. Cuypers, G. van Oldenborgh, R. Rückl, CERN-TH 6742/92 (1992). *Nucl. Phys.* **B383** (1992) 45.

[110] See, for example, P. H. Frampton, *Mod. Phys. Lett.* **A7** (1992) 2017, and the contributions of C. Heusch and P. H. Frampton to the *Proceedings of the Second International Workshop on Physics and Experiments with Linear Colliders*, Waikoloa, Hawaii (1993), Ed. F. A. Harris *et al.*, World Scientific.

[111] V. Del Duca, S. J. Brodsky, and P. Hoyer, *Phys. Rev.* **D46** (1992) 931.

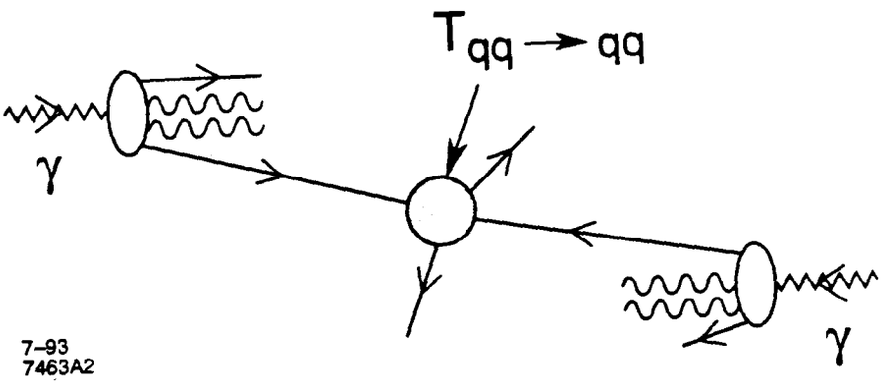

Fig. 1

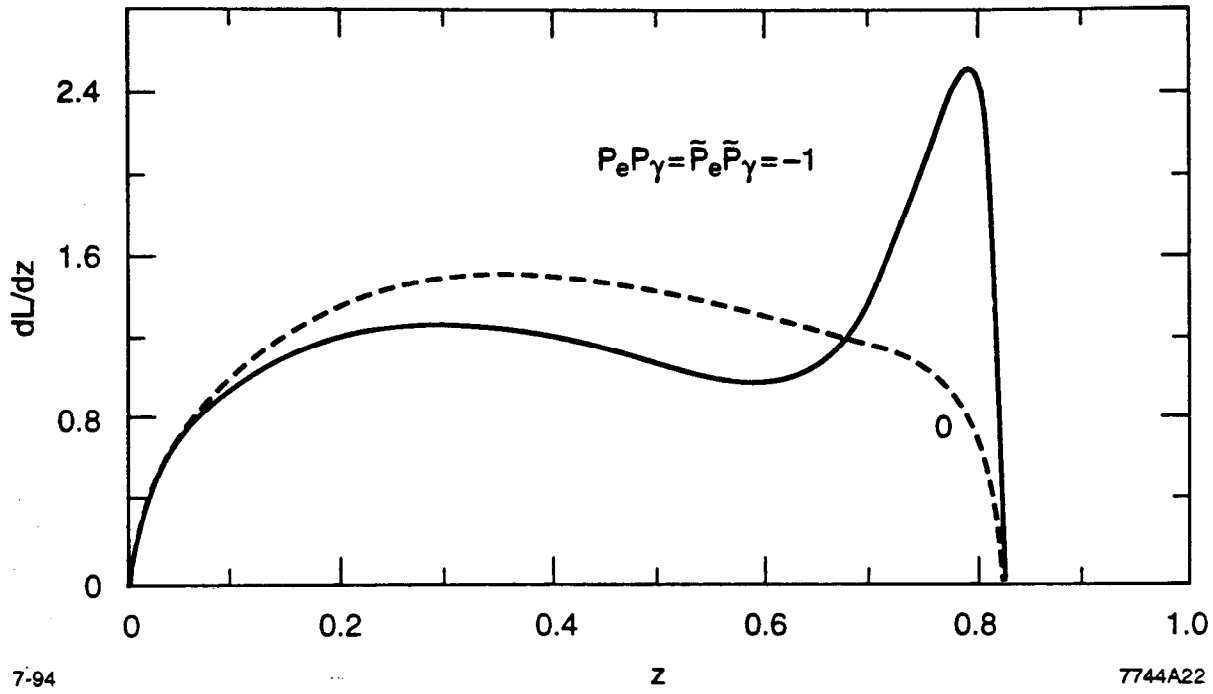
2.4
1.6
0.8
0
dL/dz
$P_eP_\gamma=\tilde{P}_e\tilde{P}_\gamma=-1$
0
0
0.2
0.4
0.6
0.8
1.0
z
7-94
7744A22

Fig. 2

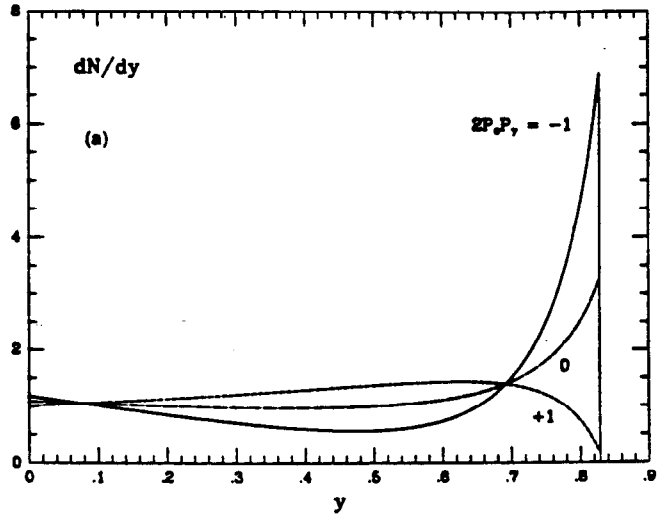
dN/dy
(a)
$2P_eP_\gamma = -1$
0
+1
y

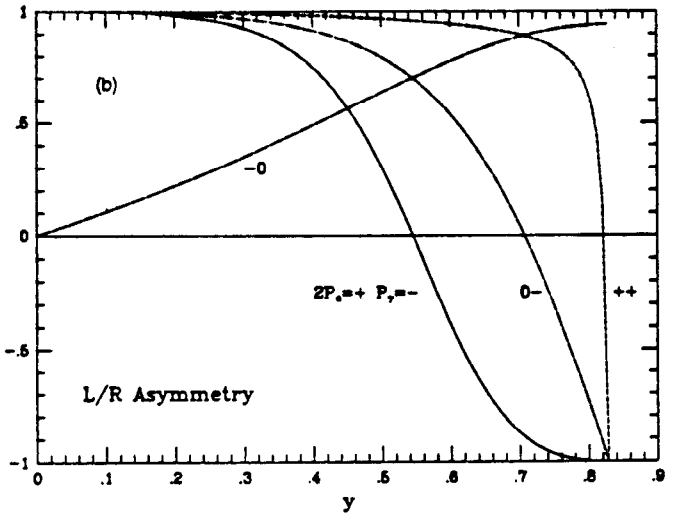
(b)
−0
$2P_e$=+ P_γ=−
0−
++
L/R Asymmetry
y

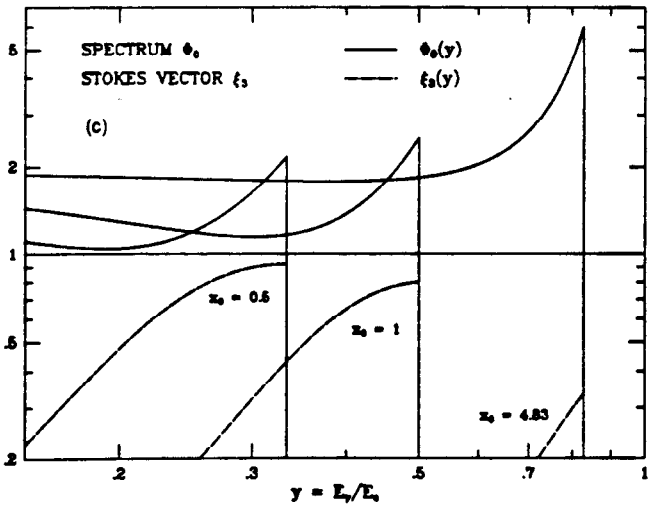
SPECTRUM Φ_0
STOKES VECTOR ξ_3
$\Phi_0(y)$
$\xi_3(y)$
(c)
$x_0 = 0.6$
$x_0 = 1$
$x_0 = 4.83$
$y = E_\gamma/E_0$

Fig. 3

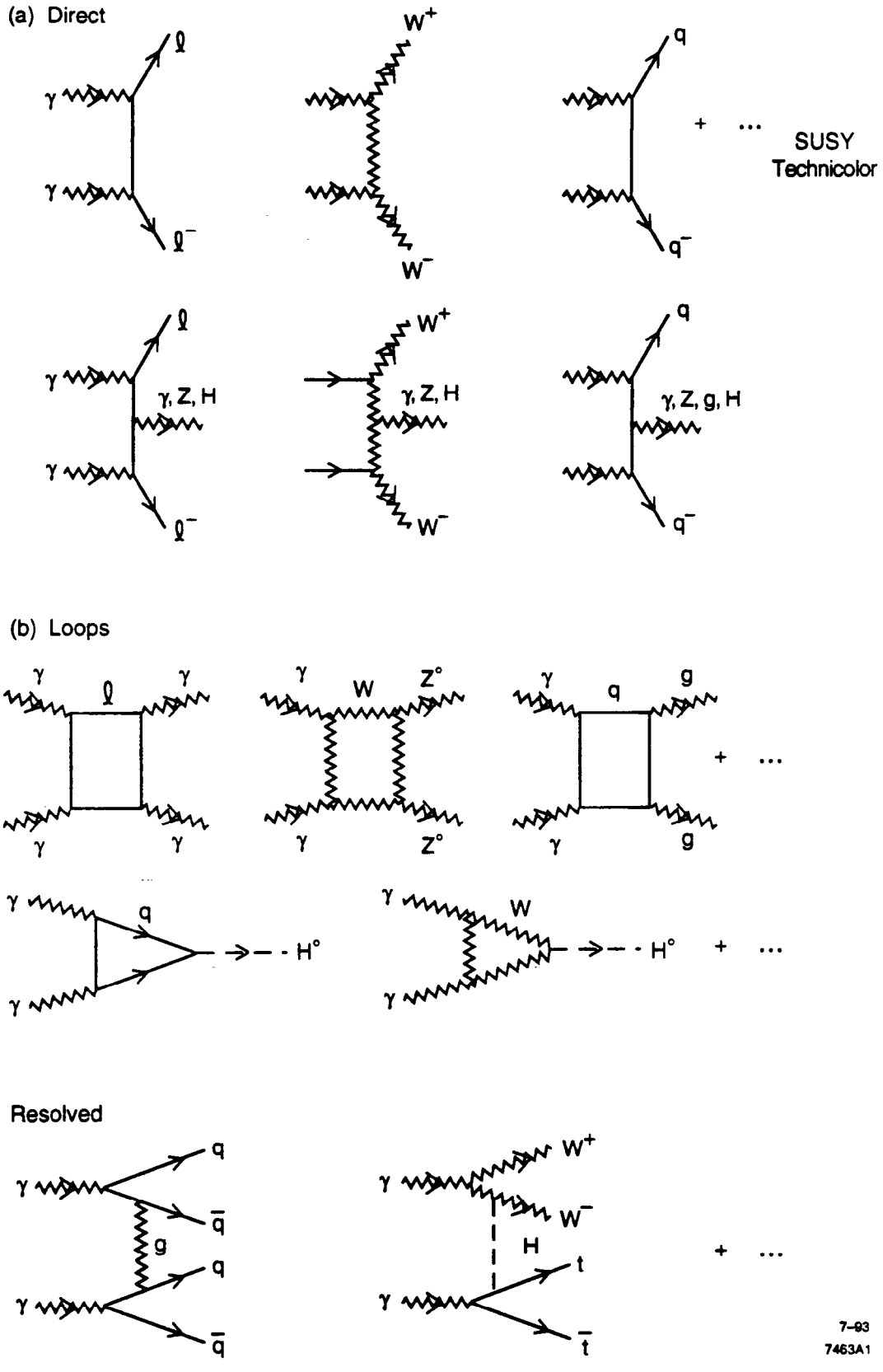
(a) Direct
ℓ
γ
γ
ℓ⁻
W⁺
W⁻
q
q⁻
+ ...
SUSY
Technicolor
γ, Z, H
γ, Z, g, H
(b) Loops
W
Z°
g
H°
(c) Resolved
q
g
t
t̄
7-93
7463A1

Fig. 4

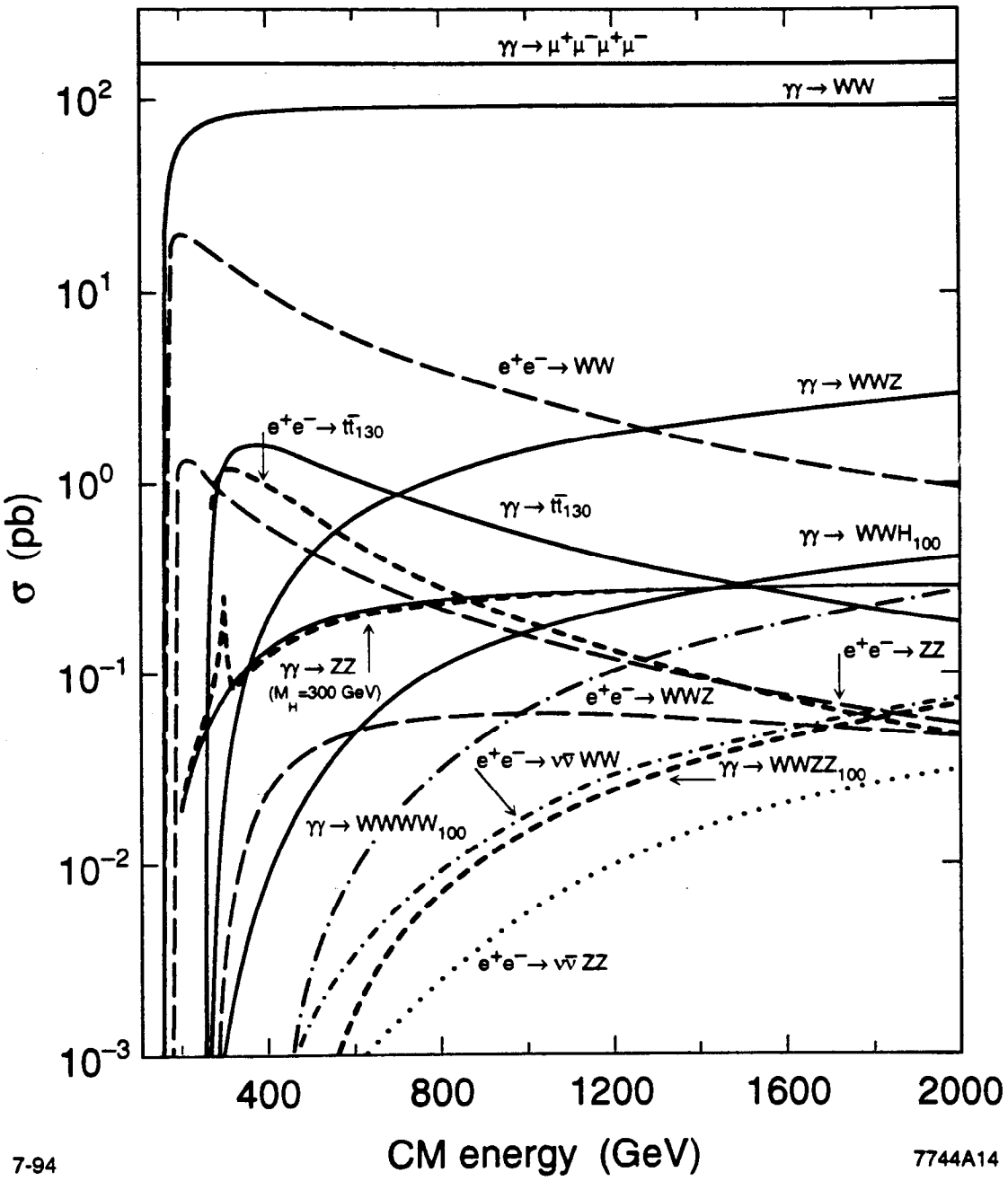
γγ → μ⁺μ⁻μ⁺μ⁻
γγ → WW
e⁺e⁻ → WW
γγ → WWZ
e⁺e⁻ → tt̄130
γγ → tt̄130
γγ → WWH100
γγ → ZZ
(MH=300 GeV)
e⁺e⁻ → ZZ
e⁺e⁻ → WWZ
e⁺e⁻ → νν̄ WW
γγ → WWZZ100
γγ → WWWW100
e⁺e⁻ → νν̄ ZZ
σ (pb)
10²
10¹
10⁰
10⁻¹
10⁻²
10⁻³
400
800
1200
1600
2000
CM energy (GeV)
7-94
7744A14

Fig. 5

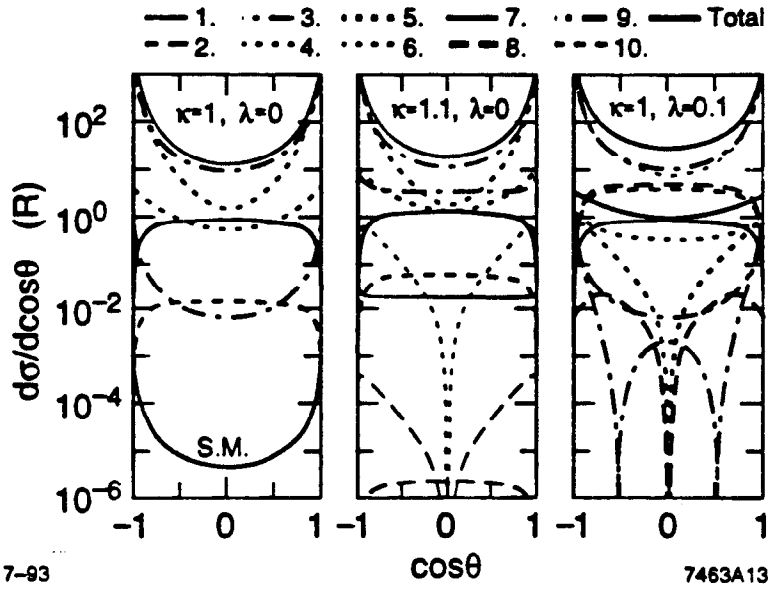
1.
2.
3.
4.
5.
6.
7.
8.
9.
10.
Total
κ=1, λ=0
κ=1.1, λ=0
κ=1, λ=0.1
S.M.
dσ/dcosθ (R)
10^2
10^0
10^-2
10^-4
10^-6
-1
0
1
cosθ
7-93
7463A13

Fig. 6

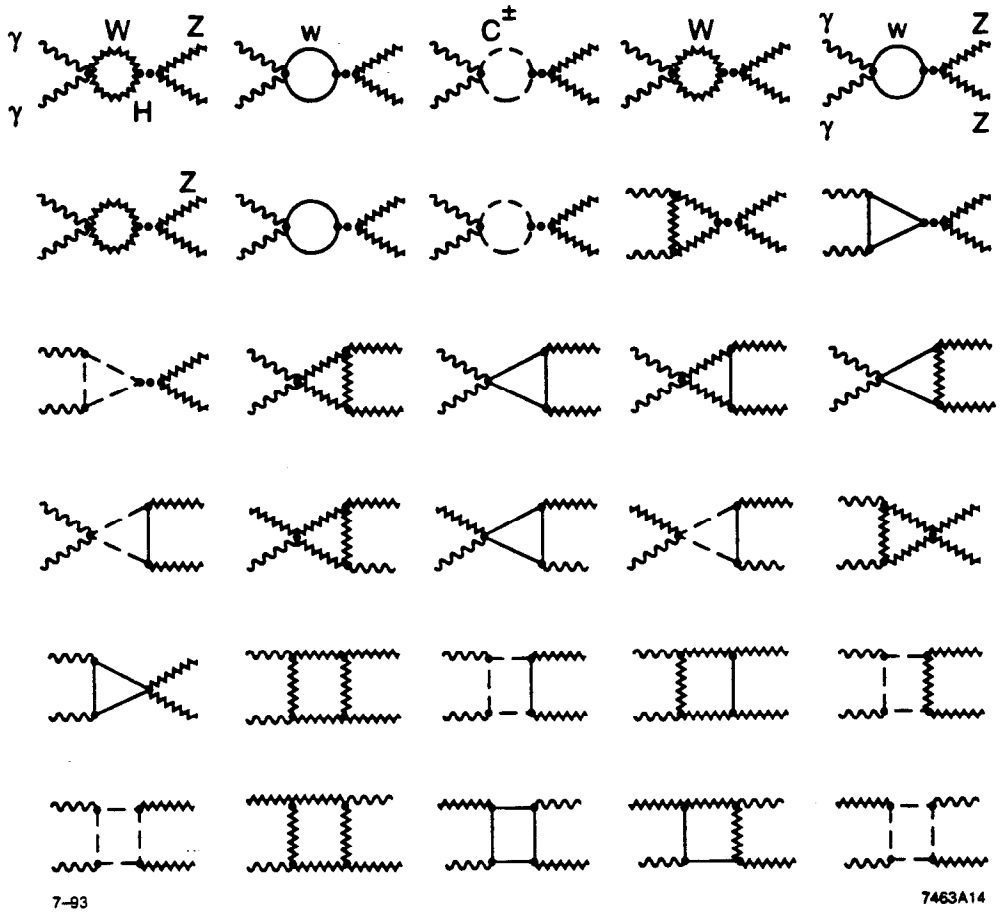

Fig. 7

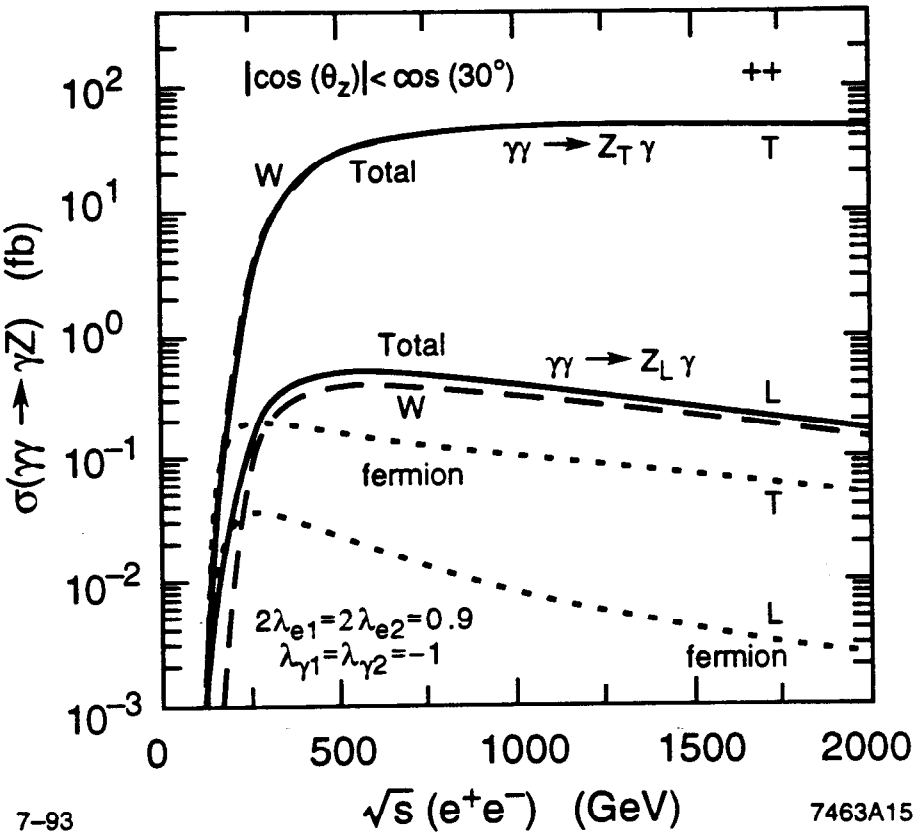
$|\cos(\theta_z)| < \cos(30°)$
++
$\gamma\gamma \rightarrow Z_T\gamma$
T
W
Total
Total
$\gamma\gamma \rightarrow Z_L\gamma$
L
W
fermion
T
L
fermion
$2\lambda_{e1}=2\lambda_{e2}=0.9$
$\lambda_{\gamma1}=\lambda_{\gamma2}=-1$
$\sigma(\gamma\gamma \rightarrow \gamma Z)$ (fb)
10^2
10^1
10^0
10^{-1}
10^{-2}
10^{-3}
0
500
1000
1500
2000
$\sqrt{s}$ (e^+e^-) (GeV)
7-93
7463A15

Fig. 8

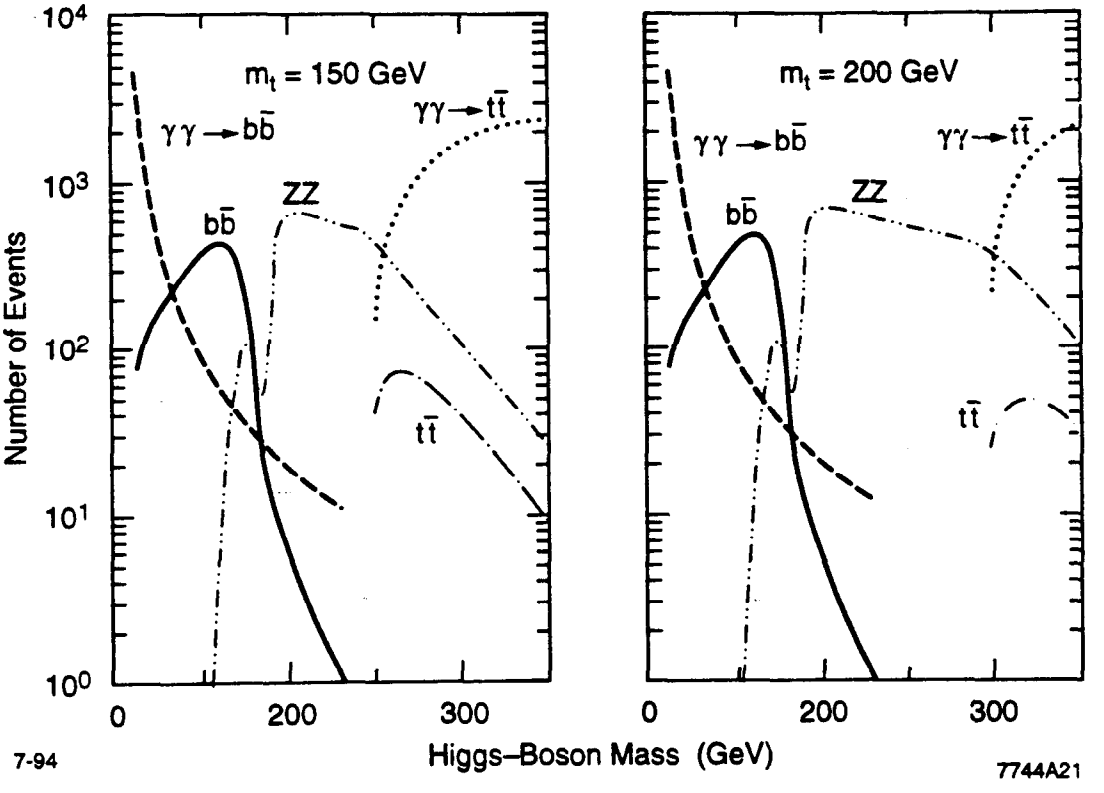
10^4
10^3
10^2
10^1
10^0
Number of Events
m_t = 150 GeV
$\gamma\gamma \rightarrow b\bar{b}$
$\gamma\gamma \rightarrow t\bar{t}$
ZZ
$b\bar{b}$
$t\bar{t}$
m_t = 200 GeV
$\gamma\gamma \rightarrow b\bar{b}$
$\gamma\gamma \rightarrow t\bar{t}$
ZZ
$b\bar{b}$
$t\bar{t}$
0
200
300
0
200
300
Higgs–Boson Mass (GeV)
7-94
7744A21

Fig. 9

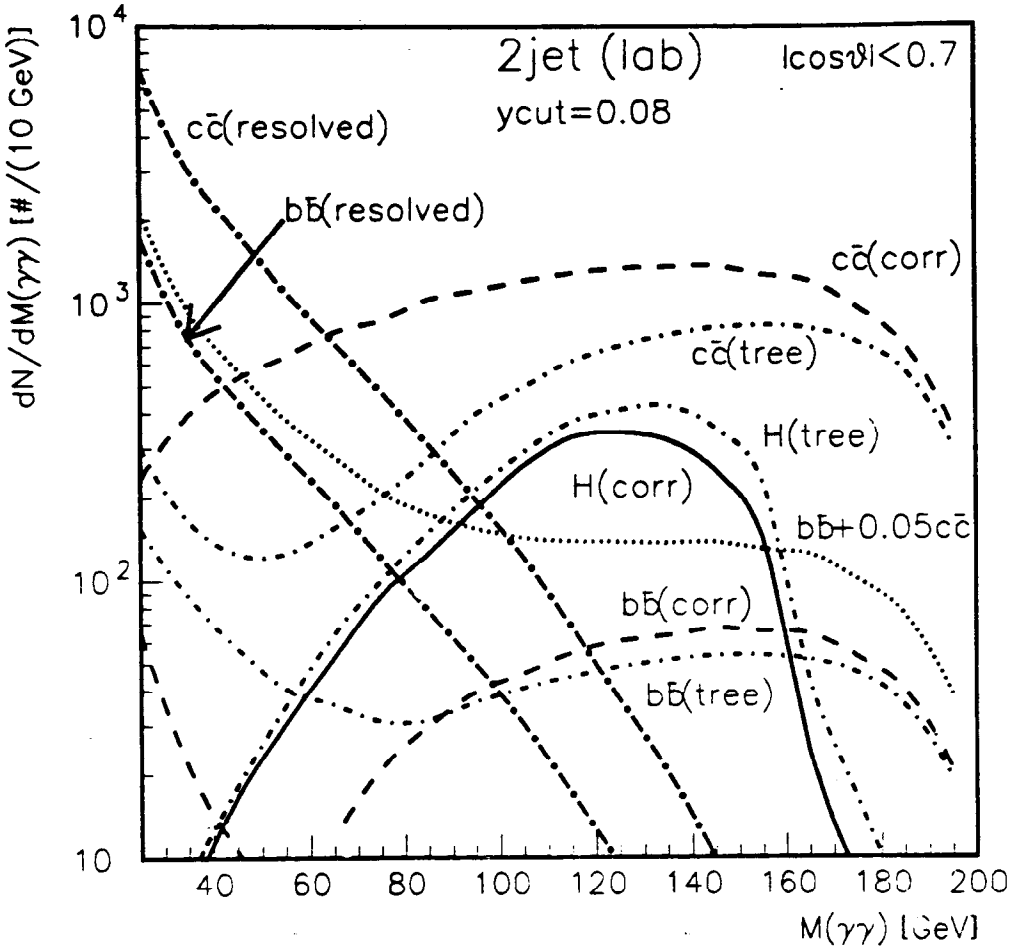
2jet (lab)
|cosϑ|<0.7
ycut=0.08
cc̄(resolved)
bb̄(resolved)
cc̄(corr)
cc̄(tree)
H(tree)
H(corr)
bb̄+0.05cc̄
bb̄(corr)
bb̄(tree)
dN/dM(γγ) [#/(10 GeV)]
M(γγ) [GeV]
10^4
10^3
10^2
10
40
60
80
100
120
140
160
180
200

Fig. 10

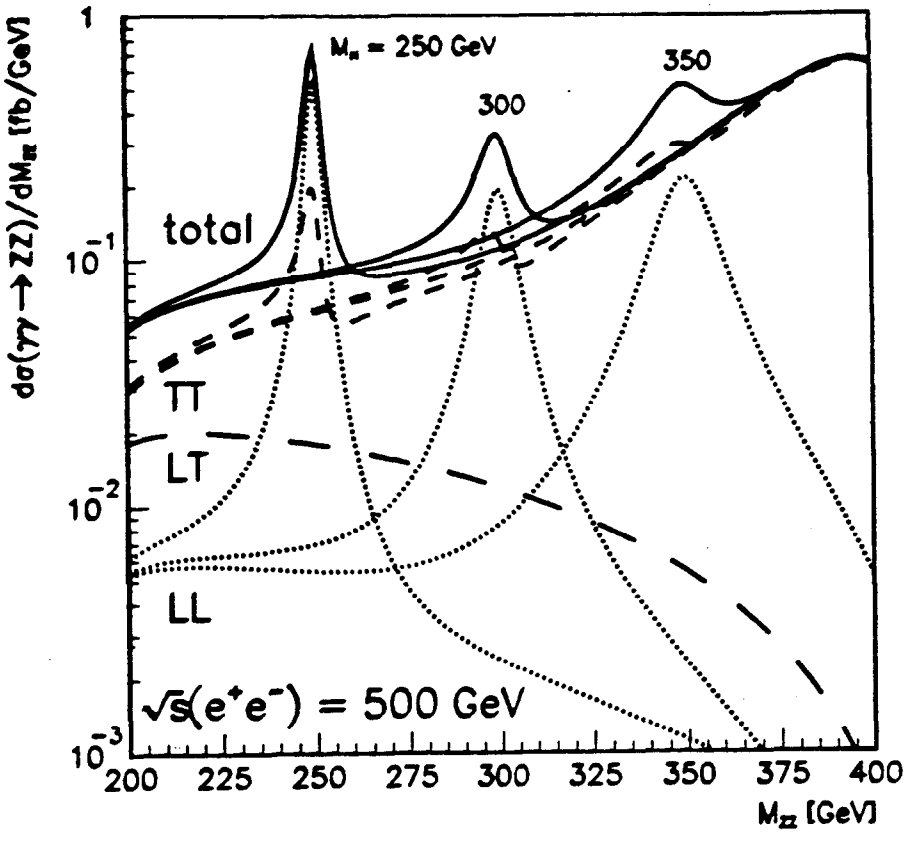
1
10^{-1}
10^{-2}
10^{-3}
$d\sigma(\gamma\gamma \to ZZ)/dM_{ZZ}$ [fb/GeV]
M_H = 250 GeV
300
350
total
TT
LT
LL
$\sqrt{s}(e^+e^-)$ = 500 GeV
200
225
250
275
300
325
350
375
400
M_{ZZ} [GeV]

Fig. 11

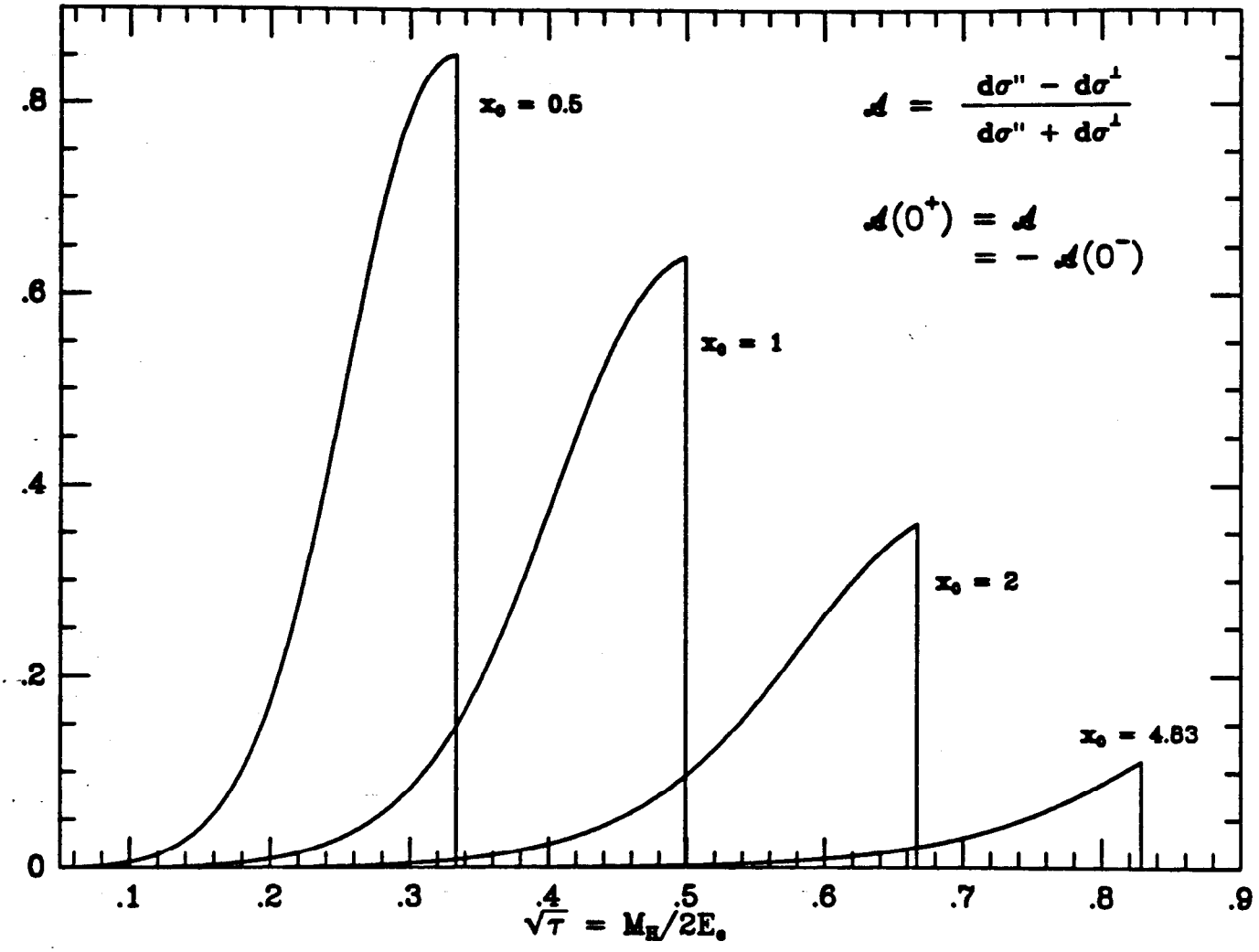
.8
.6
.4
.2
0
.1
.2
.3
.4
.5
.6
.7
.8
.9
$x_0 = 0.5$
$x_0 = 1$
$x_0 = 2$
$x_0 = 4.83$
$\mathcal{A} = \frac{d\sigma'' - d\sigma^\perp}{d\sigma'' + d\sigma^\perp}$
$\mathcal{A}(0^+) = \mathcal{A}$
$= -\mathcal{A}(0^-)$
$\sqrt{\tau} = M_H/2E_e$

Fig. 12

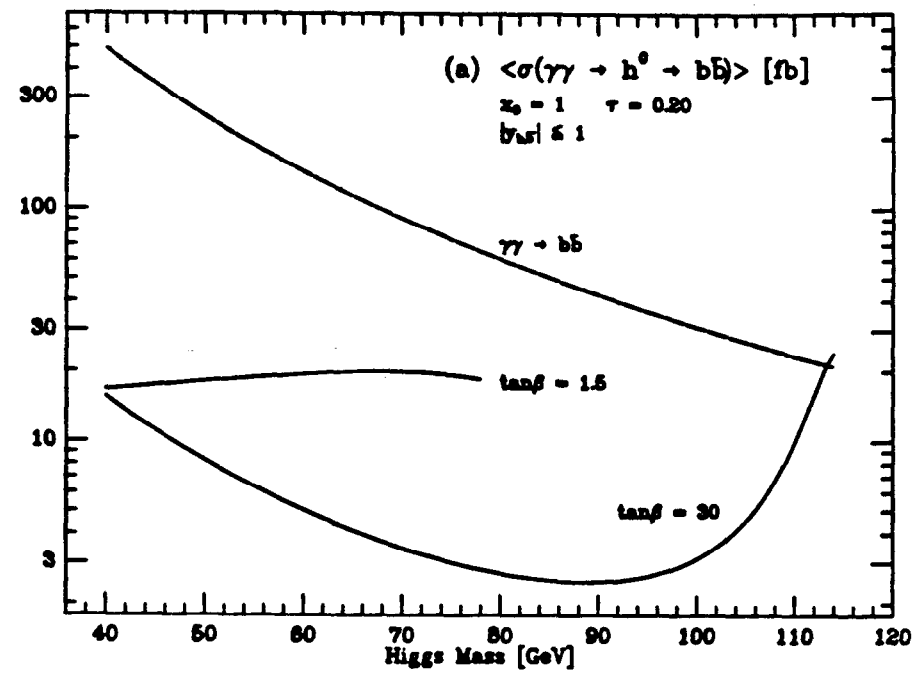
(a) <σ(γγ → h⁰ → bb̄)> [fb]
x₀ = 1 τ = 0.20
|v_hf| ≤ 1
γγ → bb̄
tanβ = 1.5
tanβ = 30
300
100
30
10
3
40
50
60
70
80
90
100
110
120
Higgs Mass [GeV]

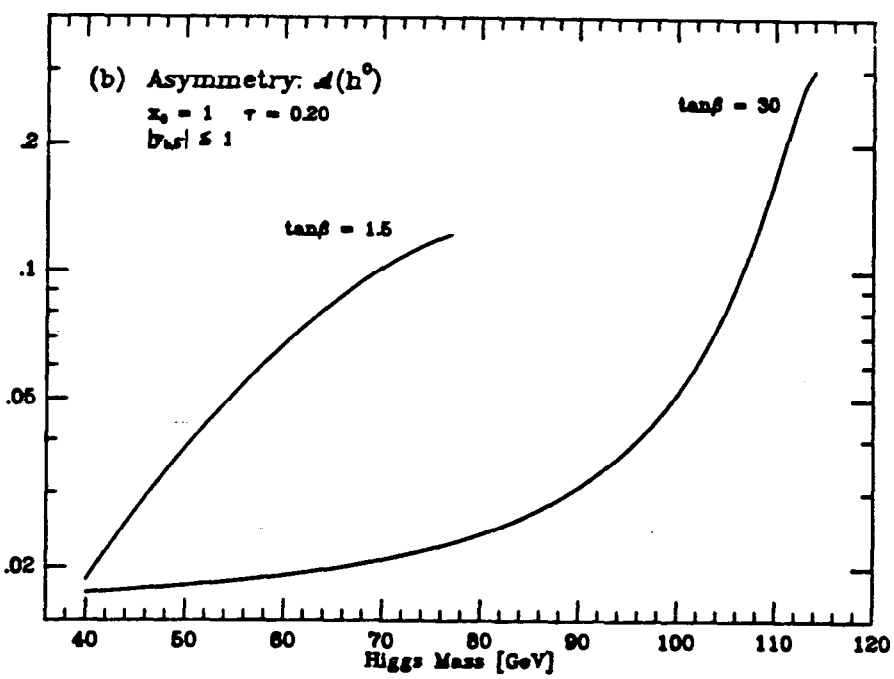
(b) Asymmetry: A(h⁰)
x₀ = 1 τ = 0.20
|v_hf| ≤ 1
tanβ = 30
tanβ = 1.5
.2
.1
.05
.02
40
50
60
70
80
90
100
110
120
Higgs Mass [GeV]

Fig. 13

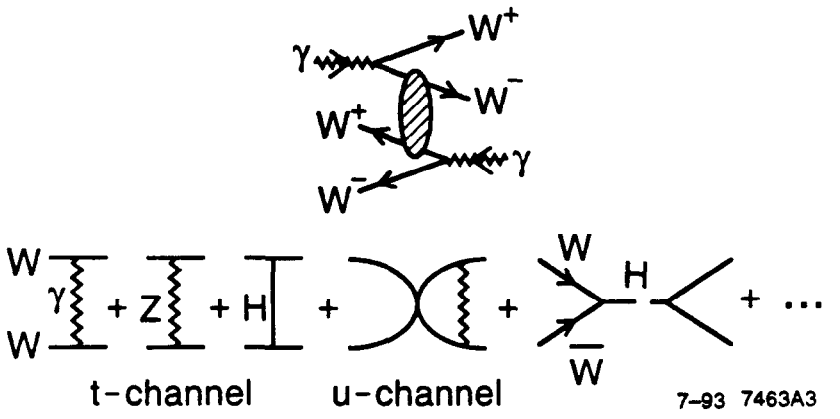

Fig. 15

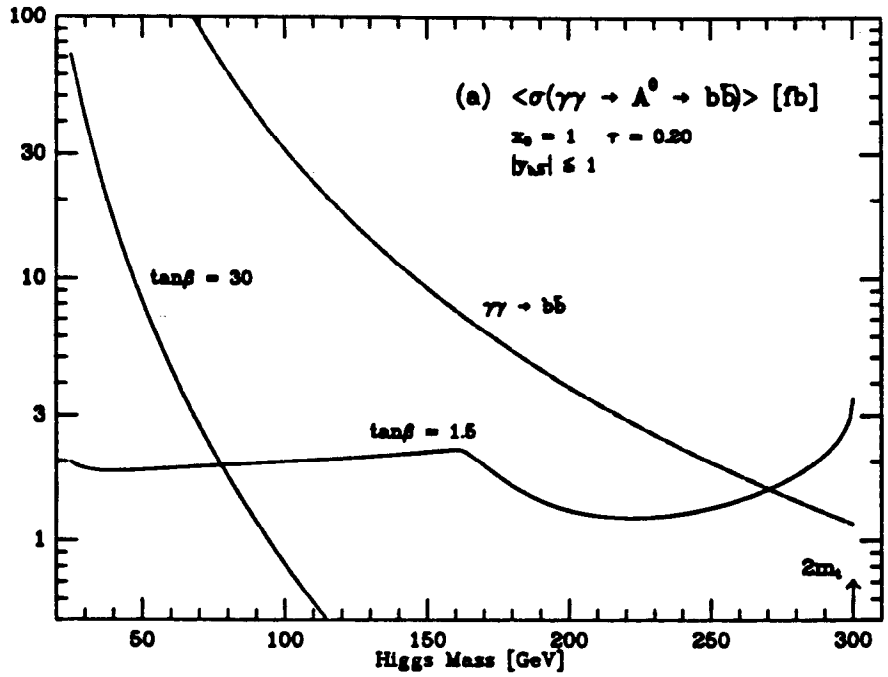
(a) $\langle\sigma(\gamma\gamma \to A^0 \to b\bar{b})\rangle$ [fb]
$x_0 = 1$ $\tau = 0.20$
$|\gamma_{LR}| \leq 1$
$\tan\beta = 30$
$\gamma\gamma \to b\bar{b}$
$\tan\beta = 1.5$
$2m_t$
100
30
10
3
1
50
100
150
200
250
300
Higgs Mass [GeV]

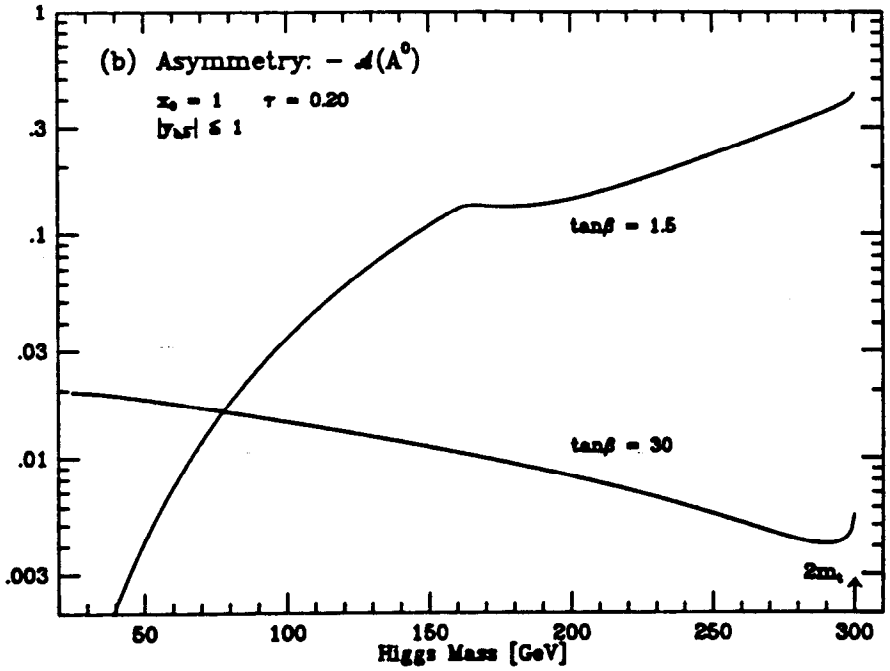
(b) Asymmetry: $-\mathcal{A}(A^0)$
$x_0 = 1$ $\tau = 0.20$
$|\gamma_{LR}| \leq 1$
$\tan\beta = 1.5$
$\tan\beta = 30$
$2m_t$
1
.3
.1
.03
.01
.003
50
100
150
200
250
300
Higgs Mass [GeV]

Fig. 14

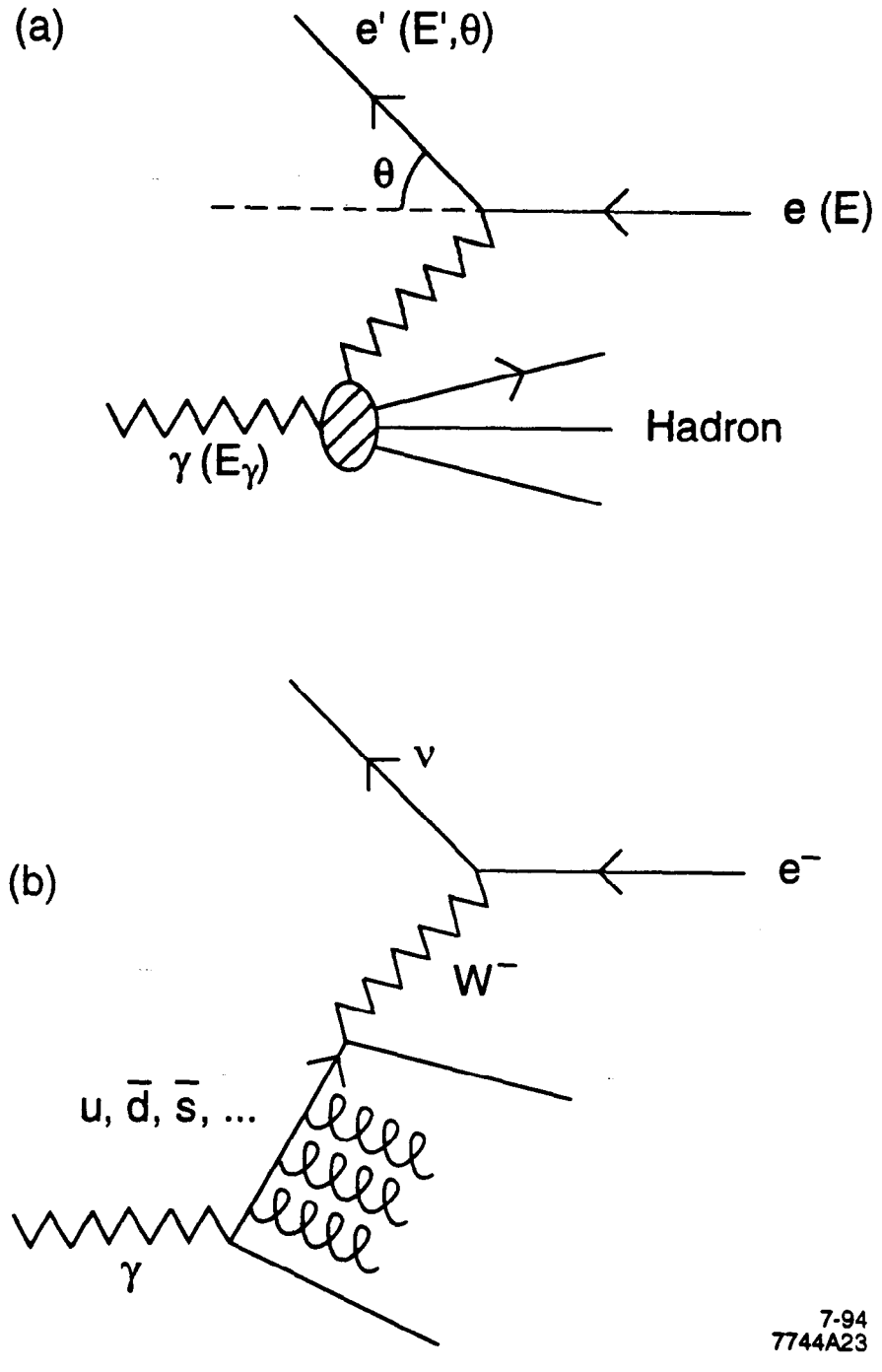

Fig. 16

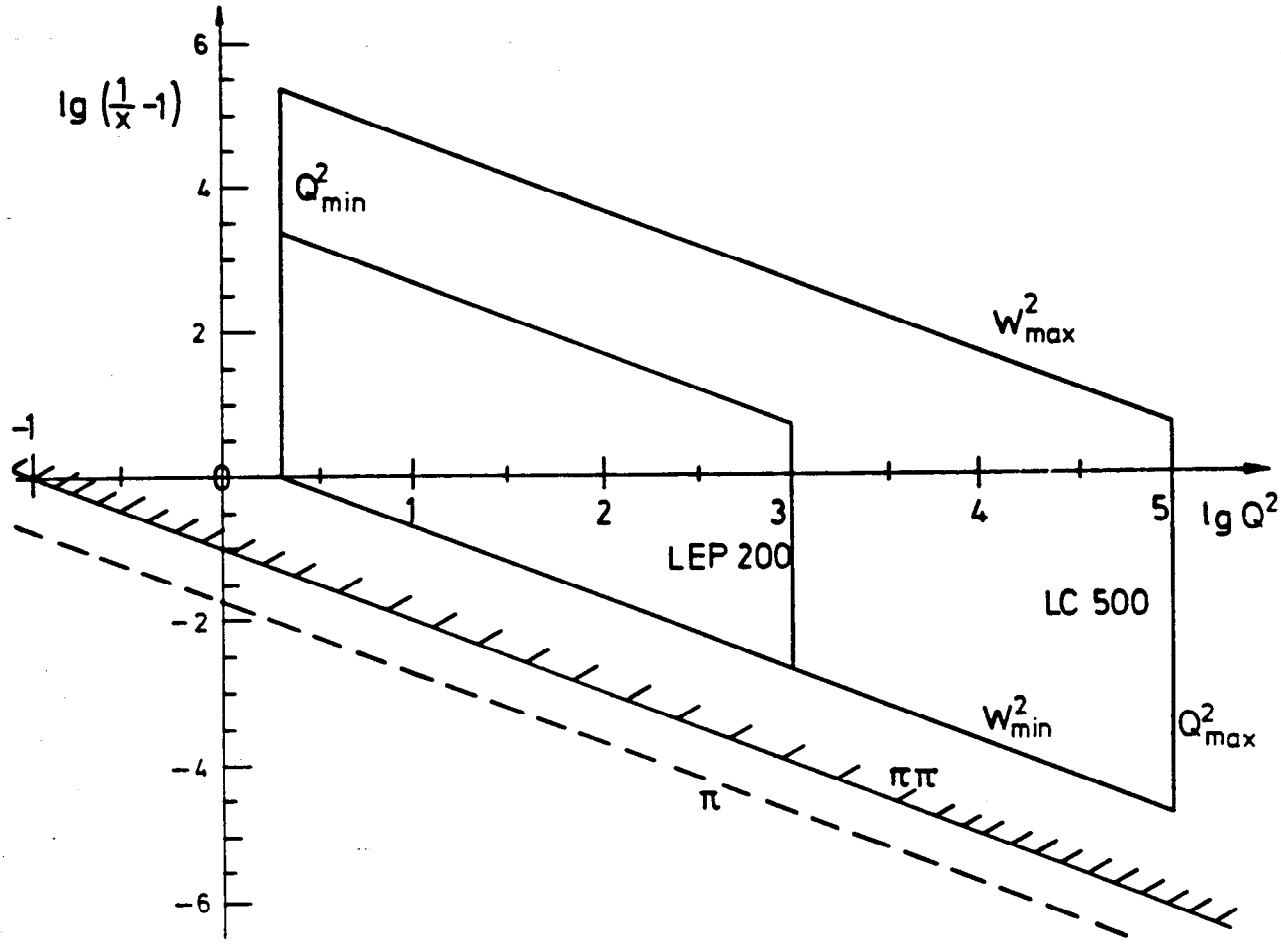
lg (1/x -1)
6
4
2
-1
0
-2
-4
-6
1
2
3
4
5
lg Q²
Q²min
W²max
W²min
Q²max
LEP 200
LC 500
ππ
π

Fig. 17

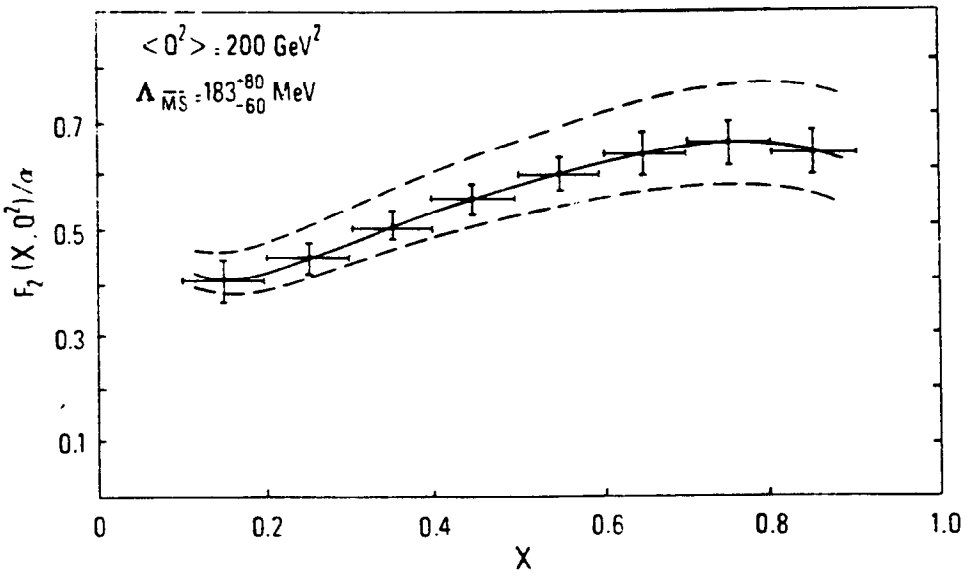
$<Q^2>$: 200 GeV^2
$\Lambda_{\overline{MS}}$: 183^{-80}_{-60} MeV
$F_2(X,Q^2)/\alpha$
0.7
0.5
0.3
0.1
0
0.2
0.4
0.6
0.8
1.0
X

Fig. 18

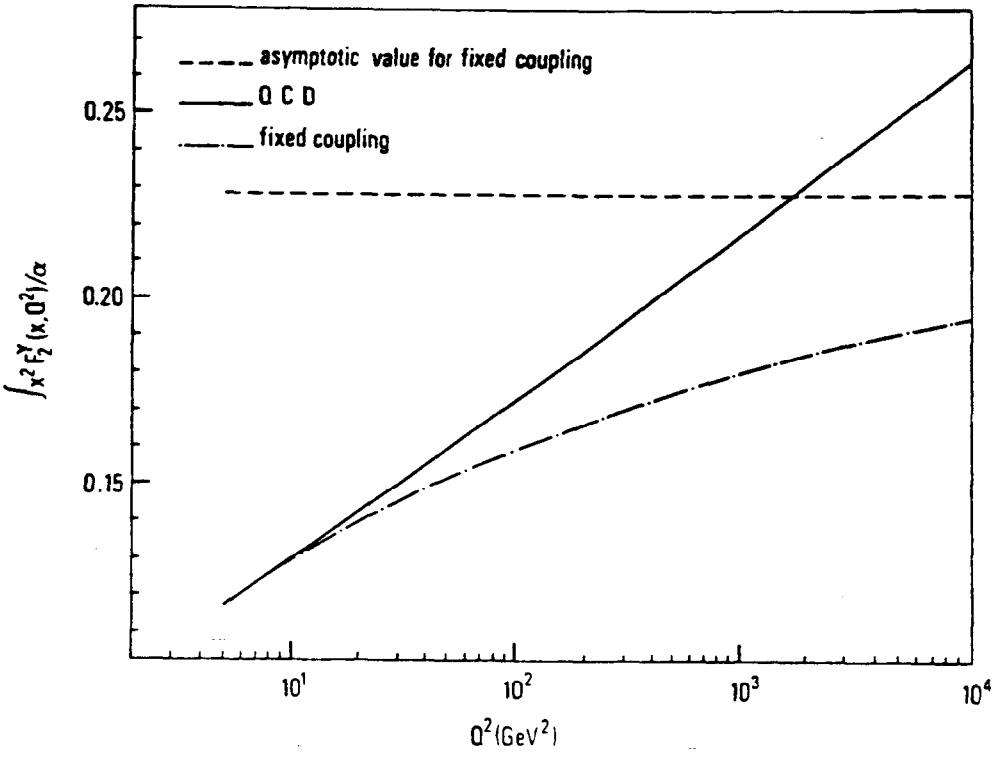
asymptotic value for fixed coupling
Q C D
fixed coupling
0.25
0.20
0.15
$\int_x F_2^\gamma(x,Q^2)/\alpha$
10^1
10^2
10^3
10^4
$Q^2(GeV^2)$

Fig 19

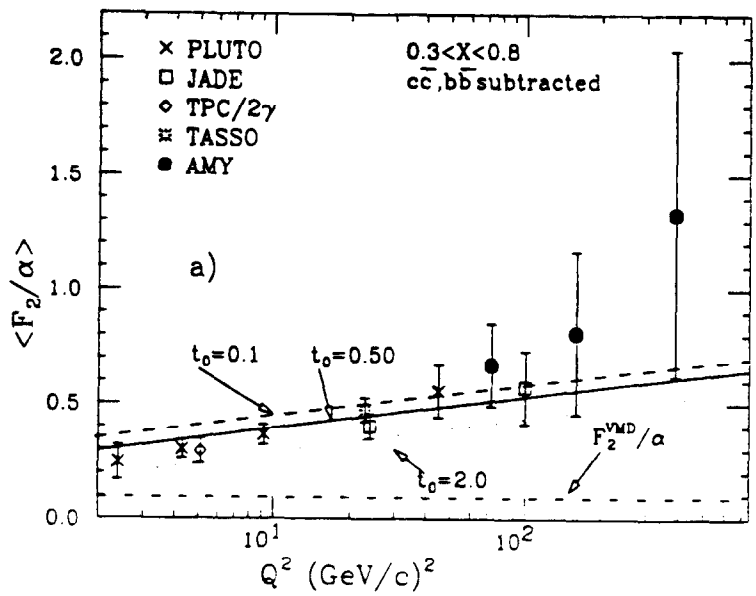
× PLUTO
□ JADE
◇ TPC/2γ
⋇ TASSO
● AMY
0.3<X<0.8
cc̄, bb̄ subtracted
a)
t_0=0.1
t_0=0.50
t_0=2.0
F_2^{VMD}/α
$<F_2/\alpha>$
Q^2 (GeV/c)^2
2.0
1.5
1.0
0.5
0.0
10^1
10^2

Fig. 20

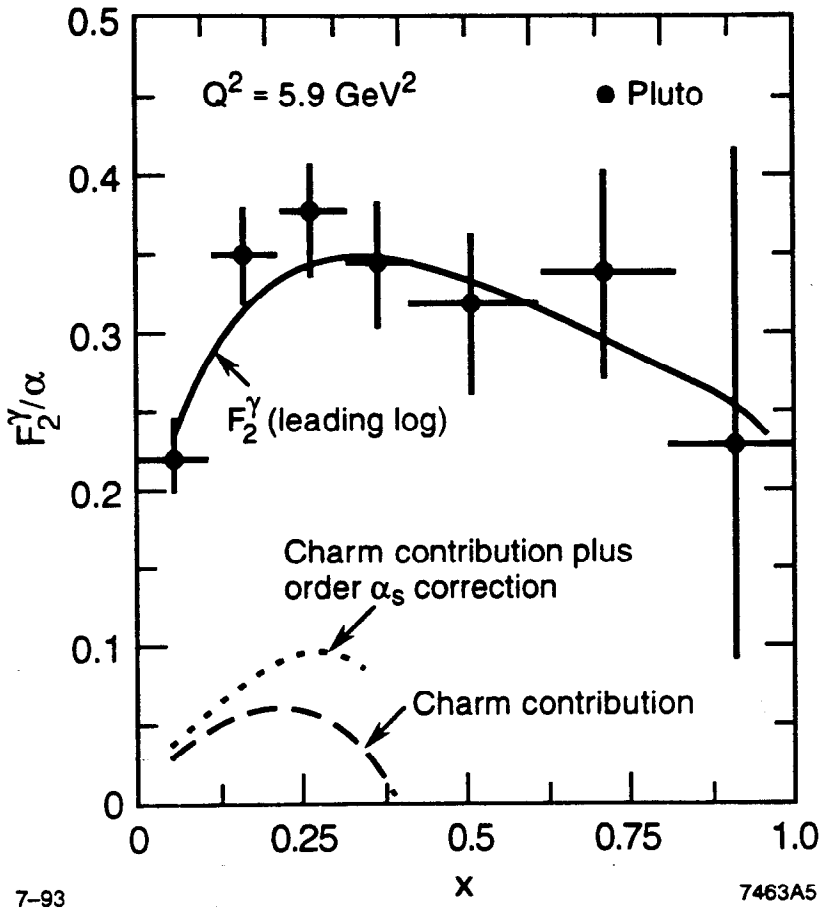
0.5
0.4
0.3
0.2
0.1
0
Q^2 = 5.9 GeV^2
● Pluto
F_2^γ/α
F_2^γ (leading log)
Charm contribution plus
order α_s correction
Charm contribution
0
0.25
0.5
0.75
1.0
x
7-93
7463A5

Fig. 21

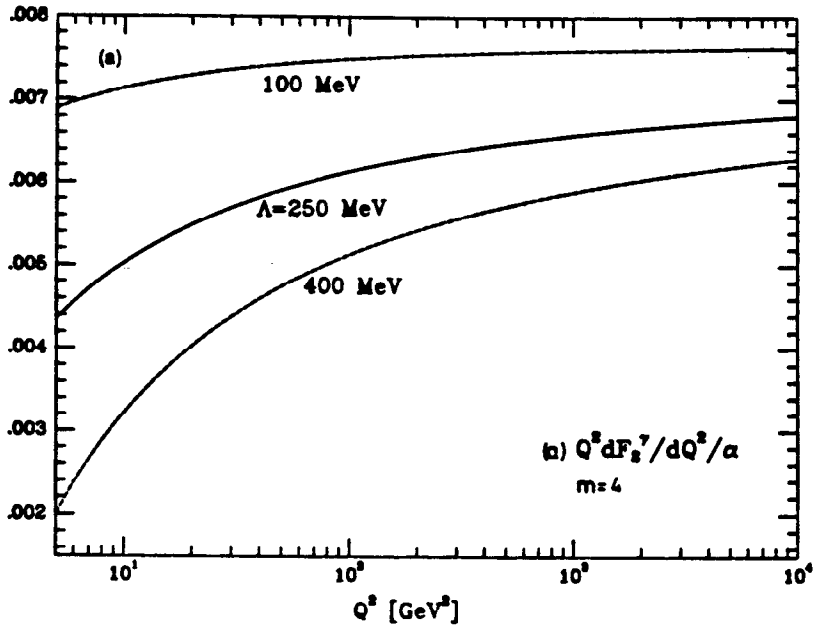
(a)
100 MeV
Λ=250 MeV
400 MeV
(a) $Q^2 dF_2^\gamma/dQ^2/\alpha$
m=4
Q^2 [GeV^2]

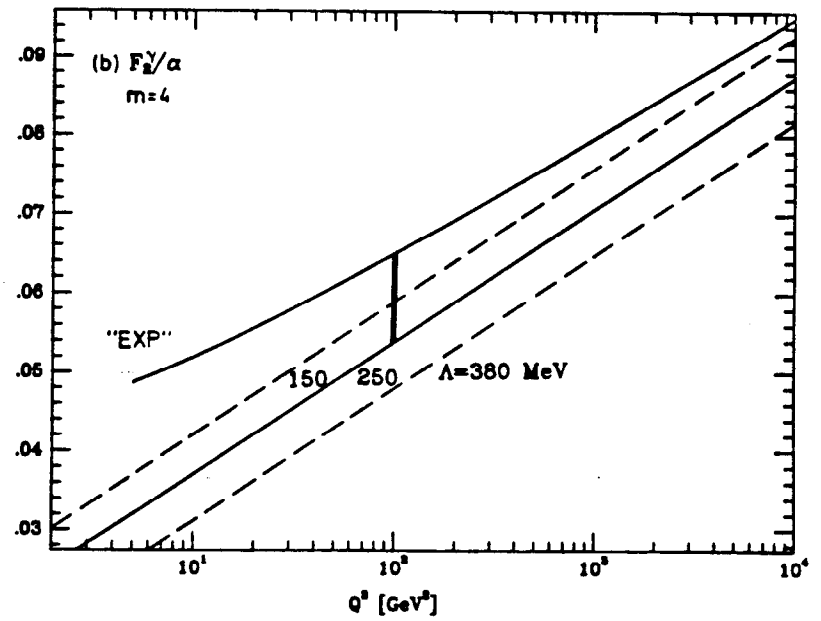
(b) F_2^γ/α
m=4
"EXP"
150
250
Λ=380 MeV
Q^2 [GeV^2]

Fig. 22

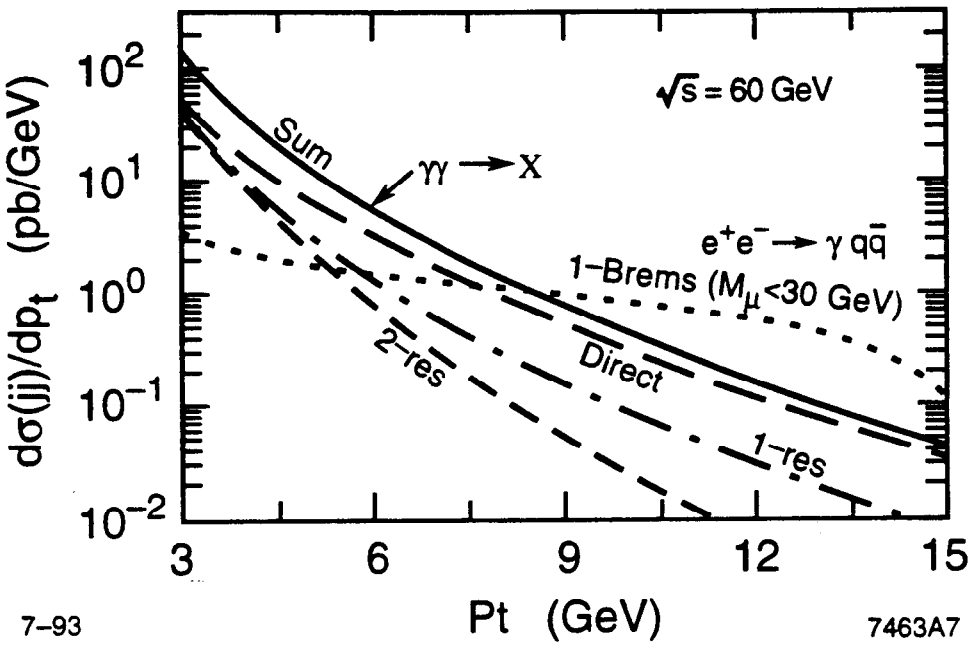
10^2
10^1
10^0
10^{-1}
10^{-2}
$d\sigma(jj)/dp_t$ (pb/GeV)
$\sqrt{s}$ = 60 GeV
Sum
$\gamma\gamma \rightarrow X$
$e^+e^- \rightarrow \gamma q\bar{q}$
1–Brems (M_μ<30 GeV)
Direct
2–res
1–res
3
6
9
12
15
Pt (GeV)
7–93
7463A7

Fig. 23

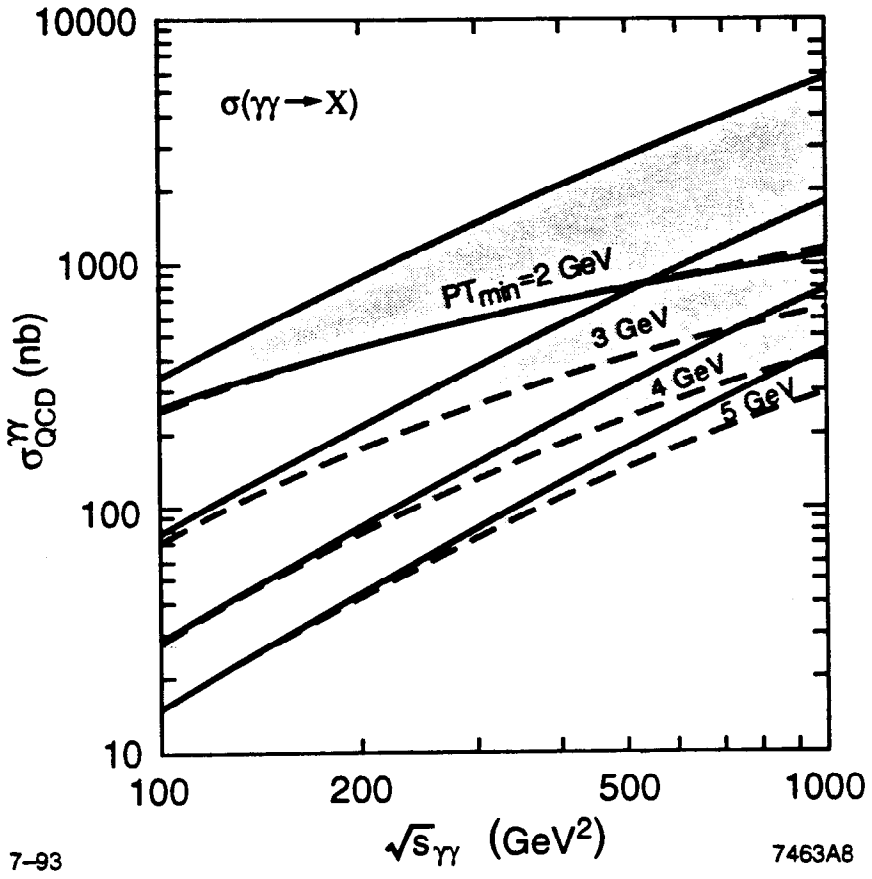
10000
1000
100
10
σ(γγ→X)
PT_min=2 GeV
3 GeV
4 GeV
5 GeV
σ^γγ_QCD (nb)
100
200
500
1000
√s_γγ (GeV²)
7-93
7463A8

Fig. 24

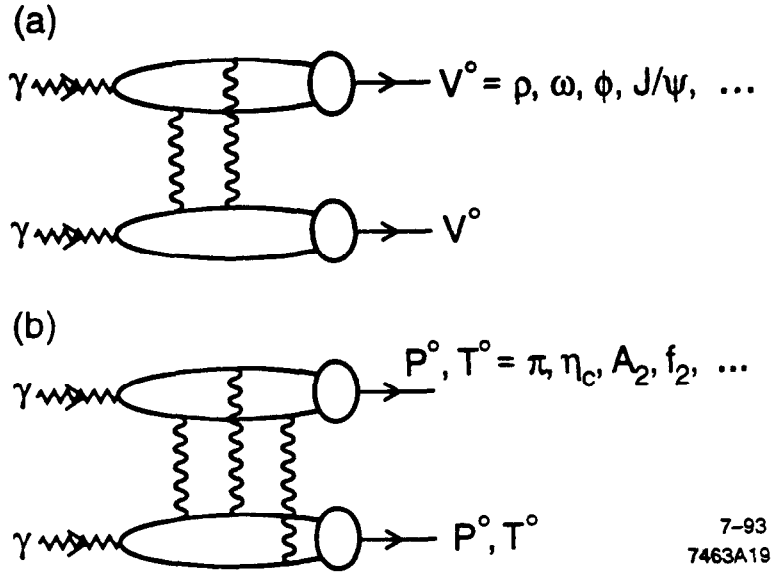

Fig. 25

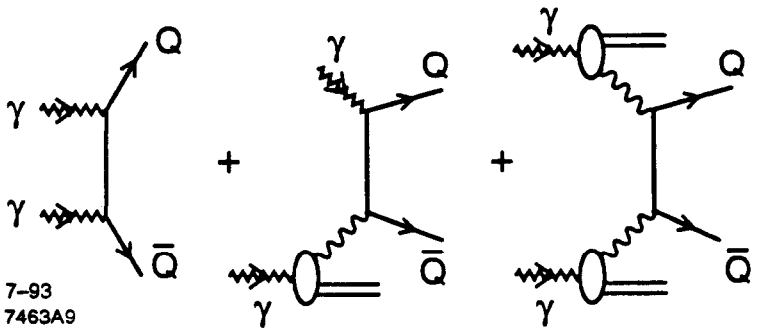

Fig. 26

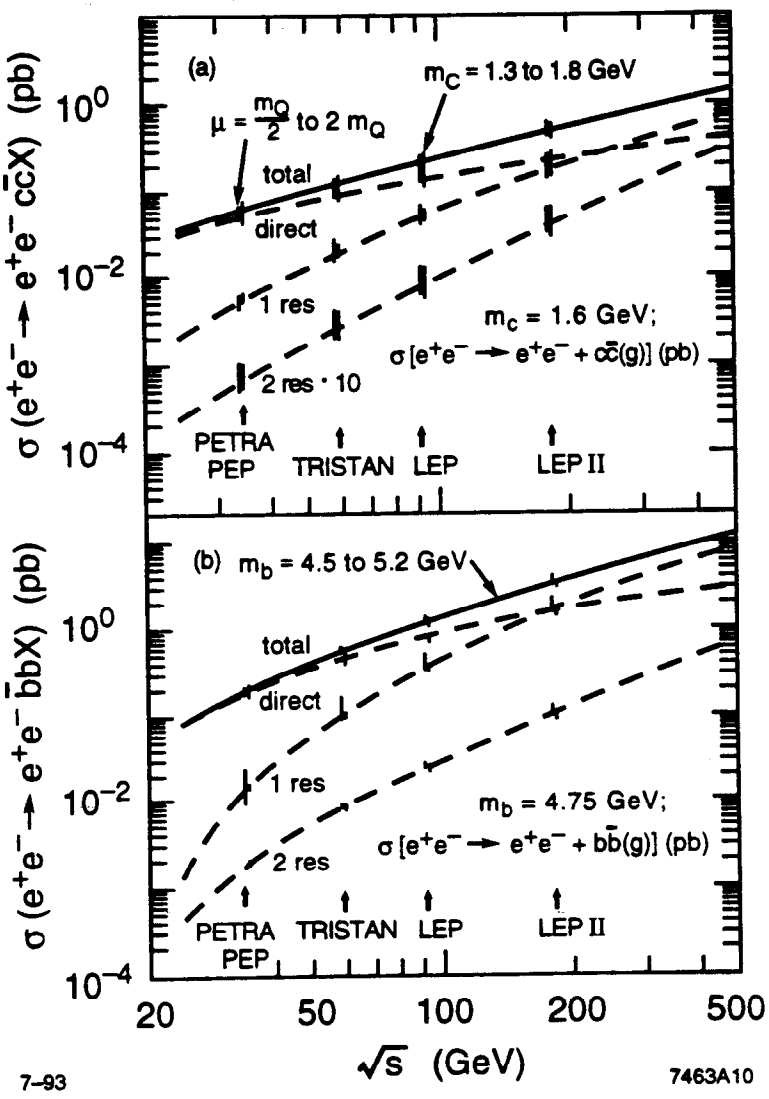
(a)
m_c = 1.3 to 1.8 GeV
$\mu = \frac{m_Q}{2}$ to 2 m_Q
total
direct
1 res
2 res · 10
m_c = 1.6 GeV;
$\sigma[e^+e^- \to e^+e^- + c\bar{c}(g)]$ (pb)
PETRA PEP
TRISTAN
LEP
LEP II
$\sigma(e^+e^- \to e^+e^- c\bar{c}X)$ (pb)
10^0
10^{-2}
10^{-4}
(b) m_b = 4.5 to 5.2 GeV
total
direct
1 res
2 res
m_b = 4.75 GeV;
$\sigma[e^+e^- \to e^+e^- + b\bar{b}(g)]$ (pb)
PETRA PEP
TRISTAN
LEP
LEP II
$\sigma(e^+e^- \to e^+e^- b\bar{b}X)$ (pb)
10^0
10^{-2}
10^{-4}
20
50
100
200
500
$\sqrt{s}$ (GeV)
7-93
7463A10

Fig. 27

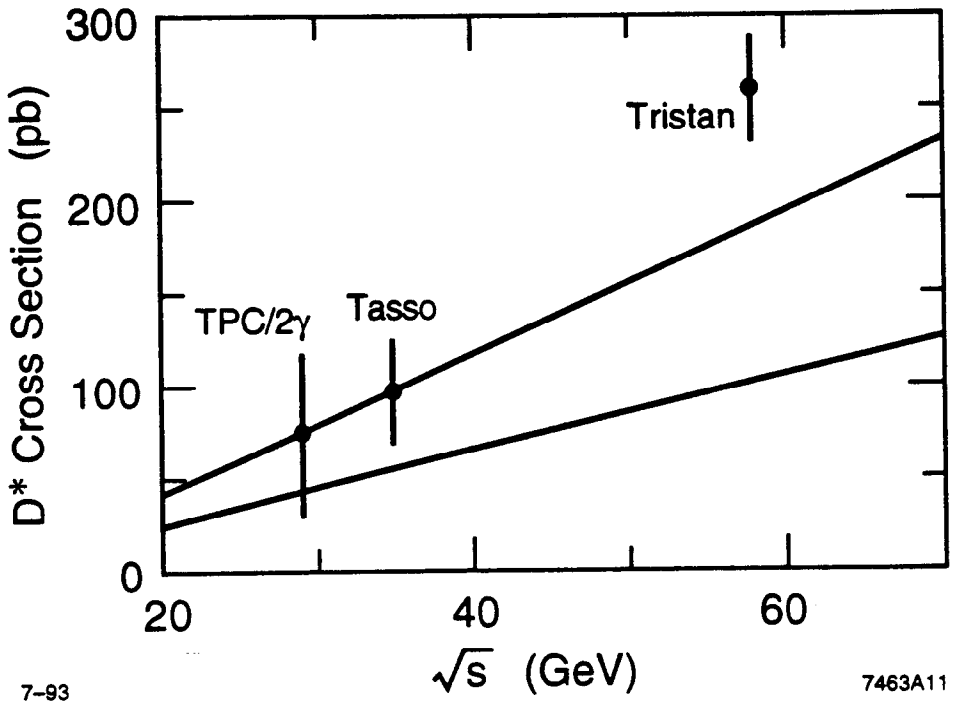
300
200
100
0
D* Cross Section (pb)
Tristan
TPC/2γ
Tasso
20
40
60
√s (GeV)
7-93
7463A11

Fig. 28

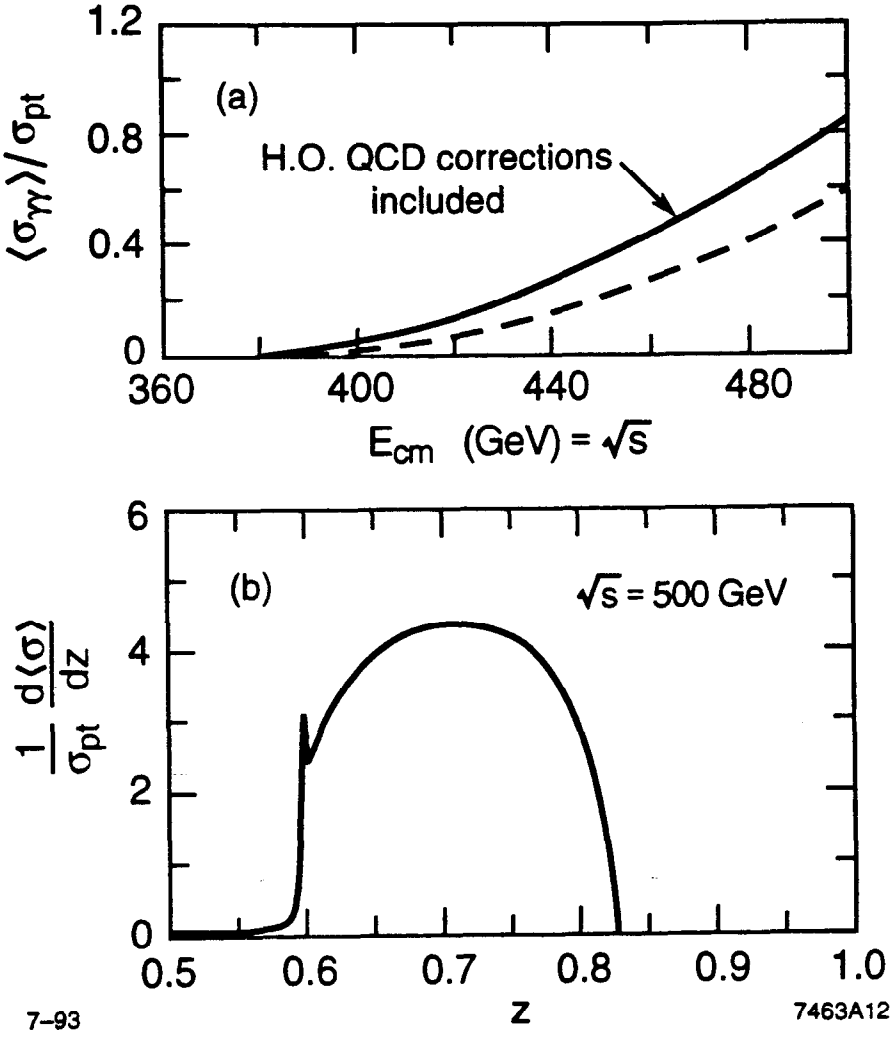
1.2
0.8
0.4
0
(a)
H.O. QCD corrections
included
$\langle\sigma_{\gamma\gamma}\rangle/\sigma_{pt}$
360
400
440
480
E_{cm} (GeV) = $\sqrt{s}$
6
4
2
0
(b)
$\sqrt{s}$ = 500 GeV
$\frac{1}{\sigma_{pt}}\frac{d\langle\sigma\rangle}{dz}$
0.5
0.6
0.7
0.8
0.9
1.0
z
7-93
7463A12

Fig. 29

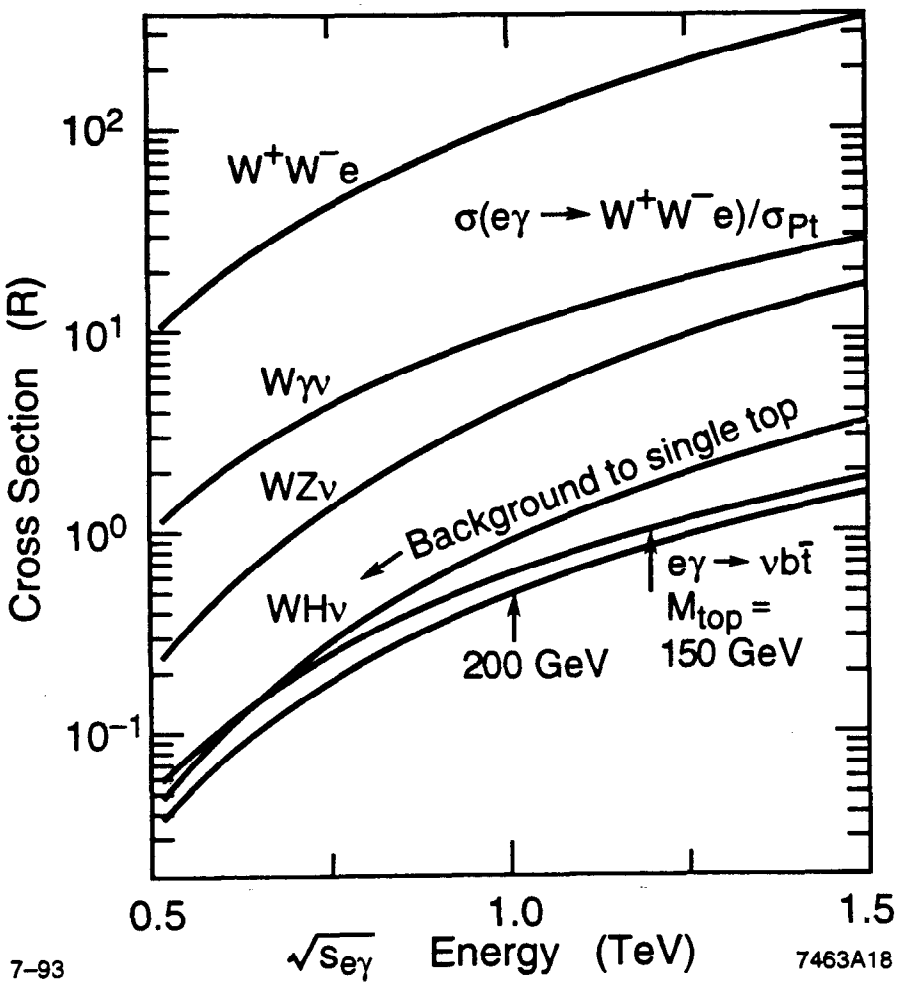
Cross Section (R)
10^2
10^1
10^0
10^{-1}
W^+W^-e
$\sigma(e\gamma \rightarrow W^+W^-e)/\sigma_{Pt}$
$W\gamma\nu$
$WZ\nu$
Background to single top
$WH\nu$
$e\gamma \rightarrow \nu b\bar{t}$
M_{top} =
150 GeV
200 GeV
0.5
1.0
1.5
$\sqrt{s_{e\gamma}}$ Energy (TeV)
7–93
7463A18

Fig. 30